Computational Geosciences (2022) 26:171–194
https://doi.org/10.1007/s10596-021-10098-3

ORIGINAL PAPER

A one-dimensional local discontinuous Galerkin Richards' equation solution with dual-time stepping

Yilong Xiao[1] · **Ethan J. Kubatko**[1] · **Colton J. Conroy**[2]

Received: 11 June 2021 / Accepted: 27 September 2021 / Published online: 3 December 2021

Abstract

We present a compact, high-order Richards' equation solver using a local discontinuous Galerkin finite element method in space and a dual-time stepping method in time. Dual-time stepping methods convert a transient problem to a steady state problem, enabling direct evaluation of residual terms and resolve implicit equations in a step-wise manner keeping the method compact and amenable to parallel computing. Verification of our solver against an analytical solution shows high-order error convergence and demonstrates the solvers ability to maintain high accuracy using low spatial resolution; the method is robust and accurately resolves numerical solutions with time steps that are much larger than what is normally required for lower-order implicit schemes. Resilience of our solver (in terms of nonlinear convergence) is demonstrated in ponded infiltration into homogeneous and layered soils, for which HYDRUS-1D solutions are used as qualitative references to gauge performance of two slope limiting schemes.

Keywords Richards' equation · Dual-time stepping · Local discontinuous Galerkin · Hydrostatic pressure

1 Introduction

Richards' equation (RE) governs single-phase, variably saturated flows driven by gravity and pressure in porous media [1]. It is commonly used to simulate soil-water flow and associated processes such as contaminant transport, land-atmosphere energy exchange, and groundwater recharge. Solving RE is complicated by a number of factors, including highly nonlinear relationships among soil hydraulic parameters, heterogeneity in soil properties, and the presence of sharp wetting fronts during infiltration into dry soils. As noted in a recent review article on the subject [2], these factors lead to several challenges in the numerical solution of RE and give rise to two main deficiencies in existing RE solvers: (*i*) A "lack of higher-order accuracy" — specifically, the authors point out that the "vast majority of spatial discretizations used in practice are based on classical low-order finite element discretizations and cell-centered finite difference;" and (*ii*) A "lack of robustness" across the range of conditions found in practice (e.g., multi-layered soils, hydrostatic pressure, capillary effects, etc) due, in part, to the "poor performance of the time integrator." Ultimately, this leads the authors of the review to conclude that "alternative solution approaches or methods are needed."

In this work, we aim to address this need through the development of a high-order RE solver based on a local discontinuous Galerkin finite-element method (LDG-FEM) in space paired with a dual-time (DT) (or pseudo-time) stepping method. There have been previous efforts utilizing DG methods for the numerical solution of RE (see, for example, [3–6]), which vary in terms of both implementation details and numerical testing of the resulting solver. However, in our estimation, although these previous DG investigations were aiming to address the lack of higher order accuracy and robustness in previous RE solvers, these deficiencies were not fully addressed in the following regards. First, with respect to high-order accuracy, while several steady-state and transient analytical solutions exist for RE, none of the previous DG investigations tested their solvers in this capacity or formally demonstrated high-order convergence rates with respect to mesh (h) refinement for RE.

✉ Yilong Xiao
xiao.76@osu.edu

Ethan J. Kubatko
kubatko.3@osu.edu

Colton J. Conroy
cjc2235@columbia.edu

[1] The Ohio State University, Columbus, OH, USA
[2] Columbia University, New York City, NY, USA

Our numerical experiments demonstrate (to our knowledge, for the first time) near-optimal high-order convergence rates with respect to h refinement for a transient analytical solution to RE. Second, with respect to robustness, the previous DG formulations were mostly tested on homogeneous soils and were not tested in the presence of hydrostatic pressure. The former scenario does not represent most natural landscapes, which are usually made up of layers of different types of soil with distinct hydraulic properties. When a fine-textured soil overlays a coarse-textured soil this can create a capillary barrier effect [7], which impedes infiltration, increases run-off, and can lead to a lack of convergence of implicit time steppers. Similarly, the latter scenario, that is, the presence of hydrostatic pressure, is also an important physical consideration when applying RE solvers to real world problems — intermittent, intense rainfall leads to ponding effects that create large pressure fronts that move through the soil and can cause instability in the numerical solver. The robustness of our specific LDG + DT formulation is demonstrated by solving problems in both of these settings (i.e., in layered soils and in the presence of hydrostatic pressure), where we show that the DT stepping approach, which hitherto has not been used in the context of RE, successfully converges in situations where other standard implicit time solvers fail.

The LDG spatial discretization, in general and in our particular formulation, possesses a number of favorable properties with regard to solving RE. First, by solving a weak form of the problem over individual elements, DG methods are able to resolve discontinuous jumps that may form in the numerical solution at the interface of layered soils typically found in nature. (This is a complication that is more difficult to resolve using high-order continuous Galerkin (CG) finite element methods). Second, the method ensures a consistent flow of information from element-to-element via a numerical flux function, which was first introduced in the context of finite volume (FV) methods. In very dry soil conditions, the RE solution for infiltration behaves similar to a “wave” of moisture traveling through the soil, where propagation speeds of the solution are finite and advective-type fluxes can be used for the numerical flux. As soil conditions increase in saturation, however, the propagation of information depends on both upstream and downstream information. To account for this wide ranging behavior we utilize a local-Lax Friedrichs (LLF) flux, which is a function of the average of the left and right states at element boundaries as well as any jump that may exist in the numerical solution and the speed with which it moves. In very dry soils, the LLF flux is similar to an upwind flux; however, in soils that are close to saturation, the LLF flux consists of a simple average. Furthermore, it is easy to implement and robust and widely used in geophysical fluid dynamics but has yet to be used in RE solvers. Our numerical results indicate that the LLF flux is robust enough to handle smooth and discontinuous transport and produces high-order solutions in infiltration, drainage, and hydrostatic pressure scenarios. Finally, unlike high-order finite difference and essentially non-oscillatory (ENO)-type spatial discretizations, the high-order spatial accuracy of DG methods is achieved without an increase in stencil width. Given this property, the pairing of DG spatial discretizations, when paired with explicit time steppers, results in a fully discrete scheme with an extremely local data structure, which, in turn, gives rise to high parallel efficiency.

However, the use of explicit time steppers present severe time step restrictions when solving RE. Implicit time stepping methods avoid this issue but result in a fully discrete scheme that compromises the compact nature and resulting parallel efficiency of DG methods. We address this issue by supplementing our DG spatial discretization with a dual time stepping (DT) method that was introduced in [8] and successfully applied to the Navier-Stokes equations [9–11]. The DT method is novel in terms of application to the RE, which are typically solved using low-order implicit steppers [2]. What makes the DT method unique is that it transforms a transient problem in physical-time to a steady-state problem in “pseudo” time by adding a pseudo-time derivative and uses the dynamical information of the flow field on shorter time scales to “time-march” to the solution at the next time level. We utilize a second-order backward difference formula to discretize physical time coupled with an explicit time stepper in “pseudo” time. By employing an explicit pseudo-time scheme, all residual terms are directly evaluated and we avoid inversion of global matrices and maintain a local data structure. This preserves the compactness of the DG method, keeping it amenable to parallel computing. Further, because the explicit time stepper uses a smaller time step in pseudo-time than in physical time, the fast waves of the problem are adequately resolved. In the context of the RE, this point is far from trivial due to the dynamics of soil moisture transport which can consist of fast moving wetting fronts in dry soils, and slow moving diffusion in saturated soils; in fact, this is frequently a sticking point in implicit methods such as the backward Euler method which can loose accuracy in the presence of sharp wetting fronts unless a small time step is used. By mixing an implicit time discretization with an explicit time stepper (in pseudo-time) we are able to converge to the solution and preserve accuracy while using a time step that is larger than what is typically achievable with standard backward difference formula.

The rest of this paper is organized as follows. First, in the next section, we introduce RE and the soil-water constitutive relations. Next, the LDG-FEM formulation and the dual-time discretization are explained. We then verify our solver against analytical solutions to demonstrate high-order accuracy as well as its robustness with respect to converging in time. We also illustrate numerical solutions under hydrostatic pressure in both a homogeneous soil column as well as a layered soil column, using HYDRUS-1D for qualitative reference. And finally, we conclude with a summary of the major findings of our work.

2 Governing equations

The governing equation is the one-dimensional (1D) mixed-form RE:

$$\frac{\partial\theta(\psi)}{\partial t}+\frac{\partial}{\partial z}\left[K(\psi)-K(\psi)\frac{\partial\psi}{\partial z}\right]=0, \tag{2.1}$$

where θ is *volumetric soil water content* (or soil water content), defined as unit volume of water per unit volume of soil, [L^3/L^3]; ψ is *soil water pressure head* (or pressure head, suction, matric potential), [L], which describes the ability of soil to absorb water. It is more negative when the soil is drier and can be positive under hydrostatic pressure; K is the hydraulic conductivity of soil, [L/T], which accounts for advective transport and is greater when soil is more saturated; z is the vertical spatial coordinate and t is time. Note that the "+" sign before the spatial derivative terms in Eq. 2.1 indicates that the vertically downward direction is taken as positive. This is the predominate direction of soil-water flows and one of the main reasons why 1D RE solvers see wide application [12–14].

Soil water constitutive relationships characterize the mathematical relationships among θ, ψ and K. For example, the Mualem-van Genuchten (MVG) model [15] describes the relationship between θ and ψ as

$$\theta(\psi)=\begin{cases}\theta_r+\frac{\theta_s-\theta_r}{[1+(\alpha|\psi|)^n]^m}, & \text{for } \psi<0;\\ \theta_s, & \text{for } \psi\geq 0,\end{cases}$$

where θ_r is the residual soil water content, [L^3/L^3], the theoretical minimum value of θ; θ_s is the saturated soil water content, [L^3/L^3], the theoretical maximum value of θ; α [L^{-1}], n [–] and m [–] are parameters that vary based on soil hydraulic properties. In the case of $\psi<0$, soil is unsaturated and the θ-ψ relationship is highly nonlinear. At $\psi=0$, soil is fully saturated and θ reaches its maximum. In a vertical infiltration scenario, ψ would exceed zero in the presence of ponding depth (hydrostatic pressure), and soil-water flow in the top saturated zone would adhere to Darcy's law until reaching the depth where $\psi\leq 0$. MVG expresses hydraulic conductivity as

$$K(\psi)=\begin{cases}K_s\cdot S_e^l\cdot\left[1-\left(1-S_e^{1/m}\right)^m\right]^2, & \text{for } \psi<0;\\ K_s, & \text{for } \psi\geq 0,\end{cases}$$

where K_s is saturated hydraulic conductivity [L/T], the theoretical maximum of K; l is an empirical curve-fitting parameter that varies based on soil properties; S_e is degree of saturation [–] which normalize θ within the range of [θ_r, θ_s]:

$$S_e=\frac{\theta-\theta_r}{\theta_s-\theta_r}.$$

In nature, soil also experiences extremely complicated hysteresis caused by different wetting and drying history. In this work, we do not consider hysteresis and assume the θ-ψ relation is unique to each type of soil.

3 Spatial discretization: local discontinuous Galerkin

3.1 Weak formulation

Equation 2.1 is rewritten as a system of first- and zero-order differential equations:

$$\frac{\partial\theta(\psi)}{\partial t}+\frac{\partial}{\partial z}\left[K(\psi)-q(\psi)\right]=0 \ \text{in}\varOmega\times[0,T], \tag{3.1a}$$

$$q(\psi)-K(\psi)r(\psi)=0 \ \text{in}\varOmega\times[0,T], \tag{3.1b}$$

$$r(\psi)-\frac{\partial\psi}{\partial z}=0 \ \text{in}\varOmega\times[0,T], \tag{3.1c}$$

where $\varOmega=\left[z_{\text{top}},z_{\text{bot}}\right]$ is the spatial domain, where z_{top} and z_{bot} denote the z coordinate of the top and bottom, respectively, of the soil column; T is the total simulation duration; $q(\psi)$ and $r(\psi)$ are auxiliary variables. Technically (3.1c) is not always necessary for a system of first-order equations, since (3.1b) can be presented as follows:

$$q(\psi)-\frac{\partial\mathfrak{K}(\psi)}{\partial z}=0,$$

where $\mathfrak{K}(\psi)$ is the anti-derivative of $K(\psi)$. In fact, this is the case in the paper which first introduced the LDG method by Cockburn and Shu [16]. However, seeking $\mathfrak{K}(\psi)$ may be overly cumbersome due to complexity of the MVG model. Hence, we resort to this alternative using three equations, as has been demonstrated by Aizinger et al. [17].

Defining a set of points $\{z_i\}_{i=0}^N$ such that $z_{\text{top}}=z_0<z_1<\cdots<z_N=z_{\text{bot}}$, the spatial domain is partitioned into a set of N elements denoted by $\varOmega_j=(z_{j-1},\ z_j)$ for $j=1,\cdots,N$ with size $\varDelta z_j=z_j-z_{j-1}$. Next, smooth test functions are defined respectively for the three equations: $\tilde{v}_\theta(z)$, $\tilde{v}_q(z)$, $\tilde{v}_r(z)$ (the subscripts indicate their corresponding solution variables). Multiplying both sides of each equation by its test function and integrating both sides over the j-th element produces a weak form of Eq. 3.1, where the strong requirement on smoothness of the independent variable and flux functions is transferred to the

test functions by an integration by parts (the independent variable is suppressed for readability):

$$\int_{\Omega_j} \frac{\partial \theta}{\partial t} \tilde{v}_\theta \, \mathrm{d}z + (K-q)\tilde{v}_\theta \Big|_{z_{j-1}}^{z_j} - \int_{\Omega_j} (K-q) \frac{\partial \tilde{v}_\theta}{\partial z} \, \mathrm{d}z = 0, \tag{3.2a}$$

$$\int_{\Omega_j} q \tilde{v}_q \, \mathrm{d}z - \int_{\Omega_j} K r \tilde{v}_q \, \mathrm{d}z = 0, \tag{3.2b}$$

$$\int_{\Omega_j} r \tilde{v}_r \, \mathrm{d}z - \psi \tilde{v}_r \Big|_{z_{j-1}}^{z_j} + \int_{\Omega_j} \psi \frac{\partial \tilde{v}_r}{\partial z} \, \mathrm{d}z = 0. \tag{3.2c}$$

Next, the following finite-dimensional space is defined:

$$\mathbb{V}_h^p = \left\{ v : \; v|_{z_{j-1}}^{z_j} \in \mathbb{Q}^p, \; \forall \Omega_j \in \mathcal{T}_h \right\},$$

where $\mathbb{Q}^p$ is the space of basis polynomials of degrees up to p and $\mathcal{T}_h$ is the partitioned spatial domain, i.e., $\mathcal{T}_h = \{\Omega_j\}_{j=1}^N$. We select our test functions denoted by $\tilde{v}_{\theta,h}$, $\tilde{v}_{q,h}$ and $\tilde{v}_{r,h}$ from $\mathbb{V}_h^p$, and we approximate θ by $\theta_h \in \mathbb{V}_h^p$. The problem described by Eq. 3.2 then becomes: to determine θ_h, q_h and $r_h \in \mathbb{V}_h^p$ such that the following system of equations holds $\forall \tilde{v}_h \in \mathbb{V}_h^p$ and $\forall \Omega_j \in \mathcal{T}_h$, i.e.,

$$\begin{aligned} \int_{\Omega_j} \frac{\partial \theta_h}{\partial t} \tilde{v}_{\theta,h} \, \mathrm{d}z = & \int_{\Omega_j} (K(\psi_h) - q_h) \frac{\partial \tilde{v}_{\theta,h}}{\partial z} \, \mathrm{d}z \\ & - (K(\psi_h) - q_h)\, \tilde{v}_{\theta,h} \Big|_{z_{j-1}}^{z_j}, \end{aligned} \tag{3.3a}$$

$$\int_{\Omega_j} q_h \tilde{v}_{q,h} \, \mathrm{d}z = \int_{\Omega_j} K(\psi_h) r_h \tilde{v}_{q,h} \, \mathrm{d}z, \tag{3.3b}$$

$$\int_{\Omega_j} r_h \tilde{v}_{r,h} \, \mathrm{d}z = - \int_{\Omega_j} \psi_h \frac{\partial \tilde{v}_{r,h}}{\partial z} \, \mathrm{d}z + \psi_h \tilde{v}_{r,h} \Big|_{z_{j-1}}^{z_j}, \tag{3.3c}$$

where the subscripts 'h' indicates that the terms are

DG approximation by the basis polynomials in $\mathbb{V}_h^p$.

The space $\mathbb{V}_h^p$ does not enforce continuity across element boundaries. Local solutions of neighbouring elements could differ at their interfaces and create dual-valued fluxes. To avoid this ambiguity, the interface terms in Eq. 3.3 are replaced with numerical fluxes, which, in general, are dependent upon the left and right limits of every element interface, i.e.

$$\begin{aligned} (K(\psi_h) - q_h)\tilde{v}_{\theta,h} \Big|_{z_{j-1}}^{z_j} \rightarrow & \left(\widehat{K}(\psi_h) - \widehat{q}_h\right)_{z_j} \left(\tilde{v}_{\theta,h}^-\right)_{z_j} \\ & - \left(\widehat{K}(\psi_h) - \widehat{q}_h\right)_{z_{j-1}} \left(\tilde{v}_{\theta,h}^+\right)_{z_{j-1}}, \end{aligned}$$

$$\begin{aligned} \psi_h \tilde{v}_{r,h} \Big|_{z_{j-1}}^{z_j} \rightarrow & \, \widehat{\psi}_{z_j} \left(\tilde{v}_{r,h}^-\right)_{z_j} \\ & - \widehat{\psi}_{z_{j-1}} \left(\tilde{v}_{r,h}^+\right)_{z_{j-1}}, \end{aligned}$$

where $\widehat{K}$, $\widehat{q}_h$ and $\widehat{\psi}$ are the numerical fluxes for $K(\psi_h)$, q_h and ψ_h, respectively, and $(\widehat{\cdot})_{z_j}$ refers to the numerical flux at z_j for $j = 1, \cdots, N$.

Some simple numerical flux schemes include arithmetic average:

$$\widehat{F}(u_z) = \frac{1}{2}\left[F(u_z^+) + F(u_z^-)\right],$$

and upwind:

$$\widehat{F}(u_z) = \begin{cases} F(u_z^-), & \text{for } \widehat{u}_z \geq 0; \\ F(u_z^+), & \text{for } \widehat{u}_z < 0, \end{cases}$$

in which F represents a generic function of u the solution variable. The numerical flux schemes we adopted are detailed in Section 5 alongside each test problem.

More implementation details on the LDG method are provided in the Appendix, such as master element transform, treatment of the constant coefficients in the test functions, the Gauss-Lobatto quadrature rule, and the computational forms of the weak form. For proof of the well-posedness of the LDG method with a formulation similar to Eq. 3.1, kindly refer to the work by Aizinger et al. [17] and the references therein.

3.2 Slope limiter

During simulation of infiltration (especially into dry soil), large pressure gradients and oscillations are expected at the wetting front. Numerical solutions could overshoot the range of $[\theta_r, \theta_s]$ and lead to erroneous flux values. This can be circumvented with the two following slope limiting schemes, which preserves local mass conservation but unfortunately reduce the order of local solutions to 1.

First is a bound-preserving limiter [18] as follows:

$$\begin{aligned} \tilde{p}_j = & \min\left\{1, \left|\frac{M - \bar{p}_j}{M_j - \bar{p}_j}\right|, \left|\frac{m - \bar{p}_j}{m_j - \bar{p}_j}\right|\right\} \\ & \cdot \left[p_j(z) - \bar{p}_j\right] + \bar{p}_j, \end{aligned} \tag{3.4}$$

where $\min\{\cdot\}$ returns the minimum entry in the brackets; p_j is the local basis-polynomial approximation of the j-th element before adjustment and $\tilde{p}_j$ is after adjustment; $\bar{p}_j$ is the local average of the j-th element; M is the global upper bound (i.e. θ_s); m is the global lower bound (i.e. θ_r); M_j and m_j are respectively the local maximum and minimum of the j-th element.

Second is the minmod limiter [19] given by

$$\tilde{p}_{j+1/2}^- = \bar{p}_j + m\left(p_{j+1/2}^- - \bar{p}_j, \; b, \; c\right), \tag{3.5a}$$

$$\tilde{p}_{j-1/2}^+ = \bar{p}_j + m\left(\bar{p}_j - p_{j-1/2}^+, \; b, \; c\right), \tag{3.5b}$$

$$b = \bar{p}_j - \bar{p}_{j-1}, \tag{3.5c}$$

$$c = \bar{p}_{j+1} - \bar{p}_j, \tag{3.5d}$$

where $p^-_{j+1/2}$ is the left limit of the $(j+1/2)$-th edge before adjustment and $\tilde{p}^-_{j+1/2}$ is after adjustment; $p^+_{j-1/2}$ is the right limit of the $(j-1/2)$-th edge before adjustment and $\tilde{p}^+_{j-1/2}$ is after adjustment; $m(\cdot)$ is the minmod function defined as

$$m(a_1, a_2, a_3) = \begin{cases} s \min\limits_{1\le n\le 3} |a_n|\,, & \text{if } s(a_1) = s(a_2) = s(a_3); \\ 0, \text{ otherwise,} \end{cases}$$

in which $s(\cdot)$ returns the sign of the parenthesized term.

The above slope limiters were selected for ease to implement and are distinct enough for performance comparison: the bound-preserving limiter stays dormant until physical bounds in θ were violated, whereas the minmod limiter actively adjusts local profiles based on solutions in neighbouring elements. For more recent breakthroughs in slope limiters for DG methods in general, refer to Kuzmin's [20] work which combines flux and slope correction. Their method has been proven for hyperbolic problems and could potentially be compatible with the elliptic-parabolic Richards' equation, but a more thorough testing of slope limiting schemes is beyond our current scope.

3.3 Hydrostatic pressure head profile

The mixed-form RE evaluates flux functions with ψ and conserves mass in θ. However, upon advancing in time, conversion of θ to ψ with the constitutive relationship discounts hydrostatic pressure because θ is capped at θ_s regardless of ψ greater than zero. To preserve the information of hydrostatic pressure, during ponded infiltration with a top-boundary pressure head of $\psi^0 > 0$, we check the saturation condition of the top soil after each time step and impose a linear pressure gradient of ψ^0/z_{sat} from the soil surface ($z = 0$) to the lower boundary of the top saturated zone ($z = z_{\text{sat}}$).

4 Temporal discretization: dual-time stepping method

This section demonstrates dual-time discretization with second-order backward difference formula (BDF2) in physical-time and forward Euler (FE) method in pseudo-time. Let (2.1) be condensed into

$$\frac{\partial \theta(\psi)}{\partial t} + R(\psi) = 0$$

where $R(\psi)$ compactly represents all the spatial terms that undergo the LDG formulation described in Section 3. We drop '(ψ)' from the time derivative because θ at the end of each physical-time step is obtained by solving for the spatial terms rather than by conversion from ψ. Instead, a conversion from θ to ψ is made at the beginning of each physical-time step for evaluation of spatial terms. Following Section 3, we make the LDG-FEM approximation $\theta_h \approx \theta$ and $\psi_h \approx \psi$:

$$\frac{\partial \theta_h}{\partial t} + R\big(\psi_h\big) = 0.$$

The physical-time derivative is discretized via BDF2 (2nd-order accurate, L-stable). As BDF2 needs known solutions from two previous time steps, we resort to a Crank-Nicolson method (2nd-order accurate, A-stable) in the first physical-time step and switch to BDF2 afterward, i.e.:

$$\begin{cases} \dfrac{\theta_h^1 - \theta_h^0}{\Delta t} + \frac{1}{2}\left[R\big(\psi_h^1\big) + R\big(\psi_h^0\big)\right] = 0, \\ \dfrac{3\theta_h^{m+1} - 4\theta_h^m + \theta_h^{m-1}}{2\Delta t} + R\big(\psi_h^{m+1}\big) = 0, \end{cases} \tag{4.1}$$

where the superscripts of θ and ψ denote physical-time level. A pseudo-time derivative, $\partial w/\partial \tau$, is added to Eq. 4.1 and discretized with forward difference. Then, all instances of θ_h^{m+1} (and θ_h^1) are replaced by $w^{(k)}$ to complete the FE discretization in pseudo-time, i.e.:

$$\begin{cases} \dfrac{w_h^{(k+1)} - w_h^{(k)}}{\Delta\tau} = \dfrac{w_h^{(k)} - \theta_h^0}{\Delta t} + \dfrac{1}{2} R_1, \\ \qquad R_1 = R\left(\psi\big(w_h^{(k)}\big)\right) + R\big(\psi_h^0\big); \\ \dfrac{w_h^{(k+1)} - w_h^{(k)}}{\Delta\tau} = \dfrac{3w_h^{(k)} - 4\theta_h^m + \theta_h^{m-1}}{2\Delta t} + R_2, \\ \qquad R_2 = R\left(\psi\big(w_h^{(k)}\big)\right), \end{cases} \tag{4.2}$$

where the superscript k indicates inner iteration level. The discretized equation in DT can be compactly written as

$$w^{(k+1)} = w^{(k)} + \Delta\tau R^*\left(w^{(k)}\right), \tag{4.3}$$

where $R^*(\cdot)$ is the dual-time residual based on right-hand-side terms in Eq. 4.2 and must turn zero as $k \rightarrow \infty$. Temporal accuracy is (almost entirely) determined by the physical-time scheme and not required for pseudo-time convergence; the only objective of inner iteration is to fulfill

$$\left| w^{(k+1)} - w^{(k)} \right| := \left| \Delta w^{(k+1)} \right| \le \epsilon \approx 0$$

for some user-defined tolerance level, ϵ. Stability condition in dual-time no longer follows the original stability condition of BDF2 or FE, but rather can be determined via a linear analysis of Eq. 4.3 in τ. For DT stepping methods with BDF2 in physical-time, the recommended stability requirement for a linear problem is $\kappa = (\Delta\tau/\Delta t) \le (2/3)$ [10, 21], where $2/3$ is the inverse of the coefficient of the unknown variable in the implicitly discretized equation using BDF2. Currently there exists no concrete methodology on estimation of optimal κ values for DT stability and convergence *a priori*. For the test problems in Section 5, optimal κ would be estimated via trial and error.

5 Tests and results

Five test problems are designed for evaluation of the LDG-DT solver. In the first three tests, the LDG-DT solver is verified against different analytical solutions. In the last two problems, HYDRUS-1D [22] (which is a well established RE solver based on continuous Galerkin FEM in space and backward Euler in time accelerated by modified Picards' method [23]) is used for qualitative comparison. Comparison is also made in each test problem between LDG-DT and LDG-BDF2 under identical spatial configurations. For all LDG-DT simulations, unless otherwise specified, convergence criterion is purposefully set to $|\Delta w| < 10^{-15}$ to demonstrate its convergence capability (this is in light of the fact that harsh convergence criterion incompatible with Δt is also a cause of incorrect convergence or non-convergence of implicit temporal schemes). Other simulation settings are detailed within the subsection of each test problem.

5.1 Infiltration toward a water table

In this problem, we rigorously assess the accuracy and h convergence rates of the DG spatial discretization and investigate the performance of the DT time stepping using a range of physical and pseudo time step sizes, comparing the results to a standard BDF2 time stepping approach.

An analytical solution for infiltration towards a water table was derived by Srivastava and Yeh [24], who adopted Gardner's [25] exponential model for hydraulic conductivity and Irmay's [26] power function for degree of saturation as follows:

$$K = K_s \cdot K_r, \tag{5.1a}$$

$$K_r = e^{\alpha_{sy}\psi} = \frac{\theta - \theta_r}{\theta_s - \theta_r}, \tag{5.1b}$$

where

$K_s = 1.0$ cm/hr is the saturated hydraulic conductivity used in their experiments; $K_r \in [0,\ 1]$ is relative hydraulic conductivity and α_{sy} [L^{-1}] is a soil-related constant. Their analytical solution for this scenario is:

$$\begin{aligned} K_r = q_B &- \left(q_B - e^{\alpha_{sy}\psi_0}\right) \cdot e^{-z} \\ &- 4(q_B - q_A) \cdot e^{(L-z)/2} \cdot e^{(-1/4)} \\ &\cdot \sum_{n=1}^{\infty} \frac{\sin(\lambda_n z)\sin(\lambda_n L) e^{-\lambda_n^2 t}}{1 + (L/2) + 2\lambda_n^2 L}, \end{aligned} \tag{5.2}$$

where

- $\alpha_{sy} = 0.1$ cm^{-1}, $\theta_r = 0.06$ and $\theta_s = 0.40$;
- $q_B = 0.9$ cm/hr is the flux at the soil surface for $t > 0$ (can be perceived as some constant rainfall rate);
- $q_A = 0.1$ cm/hr is the flux at the soil surface for $t = 0$ (initial condition only);
- $\psi_0 = 0$ cm is the pressure head at the top of the water table;
- $L = \alpha_{sy} L_*$, in which $L_* = 100$ cm is the distance to the water table from the soil surface;
- λ_n is the n-th positive root of $\tan(\lambda L) + 2\lambda = 0$, which can be numerically estimated by increasing λ from zero with tiny increment and checking for sign changes on the left-hand side. We capped n at 1000.

Srivastava and Yeh's initial condition is given by:

$$K_r(z,\ 0) = q_A - (q_A - e^{\alpha_{sy}\psi_0}) \cdot e^{(-z)}, \tag{5.3}$$

whereas the top boundary condition is:

$$q_B = \left[K_r + \frac{\partial K_r}{\partial z}\right],$$

and the bottom boundary condition is:

$$K_r = e^{\alpha_{sy}\psi_0} = 1.$$

To obtain the initial condition for LDG-DT, Eq. 5.3 is evaluated at the coordinates of all quadrature points and then converted to ψ and θ. The top boundary conditions are:

$$\widehat{\psi}_{z=0} = \psi^+_{z=0},$$
$$\left[\widehat{K} - \widehat{q}\right]_{z=0} = q_B.$$

The bottom boundary conditions are:

$$\begin{aligned} \widehat{\psi}_{z=100} &= 0, \\ \widehat{K}_{z=100} &= K_s, \\ \widehat{q}_{z=100} &= K_s \cdot r^-_{z=100}. \end{aligned}$$

At internal element interfaces, the following numerical fluxes are applied:

$$\begin{aligned} \widehat{\psi}_z &= \psi_z^+, \\ \widehat{K}_z &= \frac{1}{2}\left(K_z^+ + K_z^-\right) - \frac{|K'|}{2}\left(\theta_z^+ - \theta_z^-\right), \\ \widehat{q}_z &= K_z^- \cdot r_z^-, \end{aligned}$$

where $\widehat{K}_z$ is the local Lax-Friedrichs flux and $K' = K_s(\theta_s - \theta_r)^{-1}$ is the partial derivative of K_z with respect to θ (5.1); it corresponds to the speed of the moisture wave in very dry soil and arises from the theory of hyperbolic PDEs [27]. Spatial units are in *cm* and temporal units are in *hr*. Given that the top boundary flux (q_B) is smaller than K_s, relatively smooth profiles are expected, thus no slope limiting scheme is applied. For evaluation of accuracy, we compute the L_2 error norm against the analytical solution, i.e.:

$$\mathcal{E}_{L_2} = \left[\sum_{j=1}^{N} \int_{\Omega_j} \left(u_\mathrm{e} - u_h \right)^2 \mathrm{d}\Omega_j \right]^{1/2},$$

where u_e and u_h respectively represent the analytical and numerical solution profiles at a particular time.

Figures 1, 2 and 3 present LDG-DT solutions. The observation times are chosen for visual clarity. Accurate convergence is demonstrated at $\Delta t = 0.1$ hr, with $\Delta\tau = 0.01\Delta t$ for stability. It is plausible for the solver to converge at $\Delta t > 1$ hr, but accuracy would be compromised. The advantage of using p refinement in the LDG method in space is highlighted by the comparably accurate predictions with different combinations of spatial resolutions and basis polynomial orders: $N = 20$ with $p = 1$, $N = 5$ with $p = 2$, and $N = 2$ with $p = 4$. As reported in Table 1, near-optimal L_2 convergence rates of $p + 1$ are observed when Δt is sufficiently small [19]. Meanwhile, the use of BDF2 in physical-time will limit long-term accuracy to the second order, consequently leading to the plateauing/flattening of the curve of $p = 2$ at a later time with a larger Δt.

The selection of $\Delta\tau$ is not entirely arbitrary as it affects stability and efficiency. A general rule of thumb from the literature is that instability tends to occur when $\Delta\tau > \Delta t$, but optimization of efficiency with respect to $\Delta\tau$ and Δt is unclear [21]. For verification of our solver against analytical solutions, we define $\kappa = \Delta\tau/\Delta t$ and estimate its optimal value via trial and error. Specifically, we start with sufficiently small Δt (0.0001 hr) and κ (0.01) and compute the L_2 error at the end of a simulation. Then, we increase κ and recompute the error. If the new error is similar (on the same order of magnitude) to the initial error, the numerical results are considered to be comparably accurate. This process is repeated for increasing κ until instability or noticeably larger errors occur. Given this set of solutions, the κ corresponding to the fewest number of computational steps is reported as the “optimal” κ.

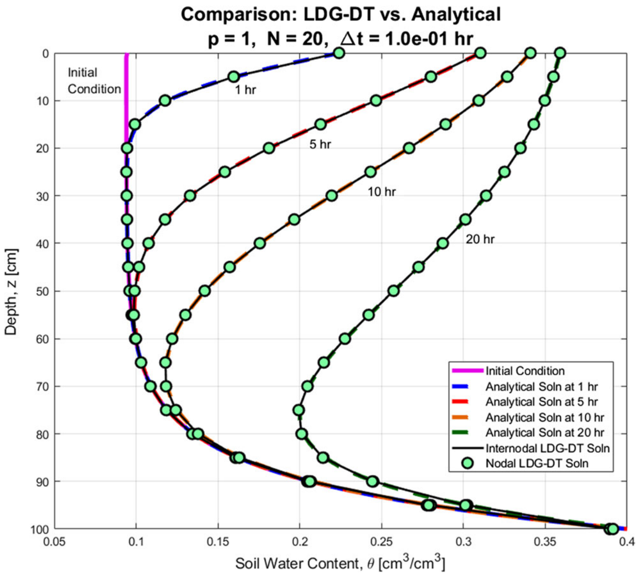

Fig. 1 Infiltration toward a Water Table: Comparison between LDG-DT ($p = 1$, $N = 20$) and analytical solutions. L_2 errors at the four observation times (ascending order) are 0.0145, 0.0141, 0.0140 and 0.0121 respectively

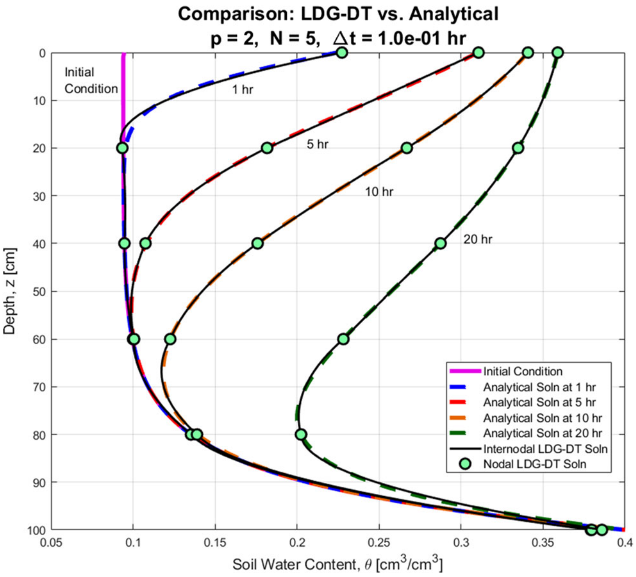

Fig. 2 Infiltration toward a Water Table: Comparison between LDG-DT ($p = 2$, $N = 5$) and analytical solutions. L_2 errors at the four observation times (ascending order) are 0.0331, 0.0299, 0.0292 and 0.0217 respectively

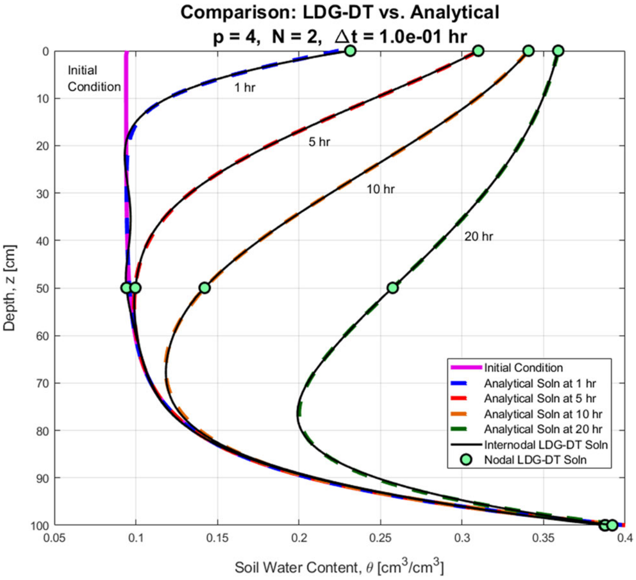

Fig. 3 Infiltration toward a Water Table: Comparison between LDG-DT ($p = 4$, $N = 2$) and analytical solutions. L_2 errors at the four observation times (ascending order) are 0.0226, 0.0176, 0.0179 and 0.0120 respectively

Table 1 L_2 Error convergence rates of LDG-DT

N	$t = [0, 1]$ hr, 10^5 Steps			$t = [5, 5.1]$ hr, 10^4 Steps		
	$p = 0$	$p = 1$	$p = 2$	$p = 0$	$p = 1$	$p = 2$
4	–	–	–	–	–	–
8	0.28	1.42	2.96	0.84	1.73	2.58
16	0.80	1.74	2.97	0.89	1.81	2.36
32	0.84	1.88	3.01	0.92	1.83	1.73
64	0.85	1.91	2.99	0.94	1.74	1.26

Near-ideal convergence rate is observed for the test from $t = 0$ hr to $t = 1$ hr. But because the method would ultimately be second-order accurate due to using BDF2 in physical-time, deterioration in convergence is expected and observed from $t = 5$ hr to $t = 5.1$ hr

Tables 2 and 3 summarize optimal κ values for a range of (physical) time steps sizes Δt. It can be noted that as Δt increases, the maximum allowable κ decreases, which agrees with previous observations in literature that $\Delta\tau < \Delta t$ is generally necessary for stability. It is also discovered that the optimal κ is very close to the maximum allowable κ (which facilitates the trial and error process); when Δt is small enough for the maximum allowable κ to be greater

Table 2 Infiltration toward a Water Table: Estimated Optimal κ for LDG-DT and Comparison against LDG-BDF2 ($N = 5$, $p = 2$, $T = 48$ hr, $\kappa = \Delta\tau/\Delta t$)

Method	ϵ	Δt (hr)	κ	Steps	$\mathcal{E}_{L_2}$
DT	10^{-6}	0.4	0.010	17588	0.0219
		0.3	0.013	16285	0.0219
		0.2	0.020	13814	0.0219
		0.1	0.040	10529	0.0219
		0.05	0.077	7905	0.0219
		0.02	**0.17**	**6133**	**0.0219**
		0.01	0.30	7087	0.0218
		0.008	0.36	7942	0.0218
		0.006	0.44	9582	0.0218
		0.004	0.55	13025	0.0218
		0.002	0.66	24740	0.0218
		0.001	0.66	48546	0.0218
		0.0005	0.66	96355	0.0218
		0.0001	0.66	480143	0.0218
BDF2	10^{-3}	≥ 0.004	–	Invalid	–
		0.002	–	24802	0.0219
		0.001	–	48570	0.0219
		0.0005	–	96573	0.0219
		0.0001	–	480000	0.0218

'Steps' is the total number of computational cycles/steps taken by the solver. For LDG-DT, this equals the summation of all pseudo-time steps in all physical-time steps; for LDG-BDF2, this equals the summation of all iterations in all physical-time steps. LDG-DT and LDG-BDF2 undergo the identical routine for spatial terms and only differ in the temporal derivatives. The most efficient run by the LDG-DT solver is emphasized in bold

'$\mathcal{E}_{L_2}$' is the L_2 error at T

'Invalid' marks unrealistic results, where at least one cell average θ value has exceeded the range of $[\theta_r,\ \theta_s]$ and led to unrealistic flux values

Table 3 Infiltration toward a Water Table: Estimated Optimal κ for LDG-DT and Comparison against LDG-BDF2 ($N = 2$, $p = 4$, $T = 48$ hr, $\kappa = \Delta\tau/\Delta t$)

Method	ϵ	Δt (hr)	κ	Steps	$\mathcal{E}_{L_2}$
DT	10^{-6}	0.4	0.010	17438	0.0122
		0.3	0.014	15415	0.0120
		0.2	0.022	13072	0.0122
		0.1	0.043	9852	0.0121
		0.05	0.085	7378	0.0121
		0.02	**0.19**	**5812**	**0.0121**
		0.01	0.32	6962	0.0120
		0.008	0.38	7892	0.0120
		0.006	0.43	9352	0.0120
		0.004	0.53	13100	0.0120
		0.002	0.66	24598	0.0120
		0.001	0.66	48558	0.0120
		0.0005	0.66	96419	0.0120
		0.0001	0.66	480090	0.0120
BDF2	10^{-3}	≥ 0.004	–	Invalid	–
		0.002	–	24003	0.0120
		0.001	–	48000	0.0120
		0.0005	–	96000	0.0120
		0.0001	–	480000	0.0120

'Steps' is the total number of computational cycles/steps taken by the solver. For LDG-DT, this equals the summation of all pseudo-time steps in all physical-time steps; for LDG-BDF2, this equals the summation of all iterations in all physical-time steps. LDG-DT and LDG-BDF2 undergo the identical routine for spatial terms and only differ in the temporal derivatives. The most efficient run by the LDG-DT solver is emphasized in bold

'$\mathcal{E}_{L_2}$' is the L_2 error at T

'Invalid' marks unrealistic results, where at least one cell average θ value has exceeded the range of $[\theta_r,\ \theta_s]$ and led to unrealistic flux values than $\approx\ 2/3$, the optimal κ would simply be $\approx\ 2/3$, which coincides with the recommended upper limit of κ for using BDF2 in physical-time, mentioned near the end of Section 4. We also loosened error tolerance from the default $\epsilon = 10^{-15}$ to $\epsilon = 10^{-6}$, which suffices for accuracy in this problem while taking far fewer computational steps. Almost identical L_2 error is observed for $\epsilon \in [10^{-15},\ 10^{-6}]$.

Also included in Tables 2 and 3 are simulation results using LDG-BDF2. An error tolerance of $\epsilon = 10^{-3}$ is used for LDG-BDF2. We noticed that smaller ϵ could lead to non-convergence. For example, Fig. 4 shows overestimation of infiltration speed with $\epsilon = 10^{-6}$, due to the fact that LDG-BDF2 fails to converge in early simulation and is forced to accept an incorrect estimation in order to advance in time (we cap the number of iterations). With reference to the LDG-DT results, it is found that at the Δt values where LDG-BDF2 starts to converge correctly, the total number of computational steps it takes is similar to LDG-DT for the same Δt. Coincidentally, the largest Δt at which LDG-BDF2 converges accurately is also where optimal $\kappa \approx 2/3$ for LDG-DT. Hence $\kappa \approx 2/3$ can be interpreted as a critical point: For Δt where optimal $\kappa < 2/3$, LDG-DT is clearly the superior choice, otherwise the two time steppers would be on par with each other (provided that Δt and ϵ for LDG-BDF2 are compatible). By plotting optimal κ against Δt in log-log scale, an almost linear trend is observed for optimal $\kappa < 2/3$ (Fig. 5), as shown in Figs. 6 and 7.

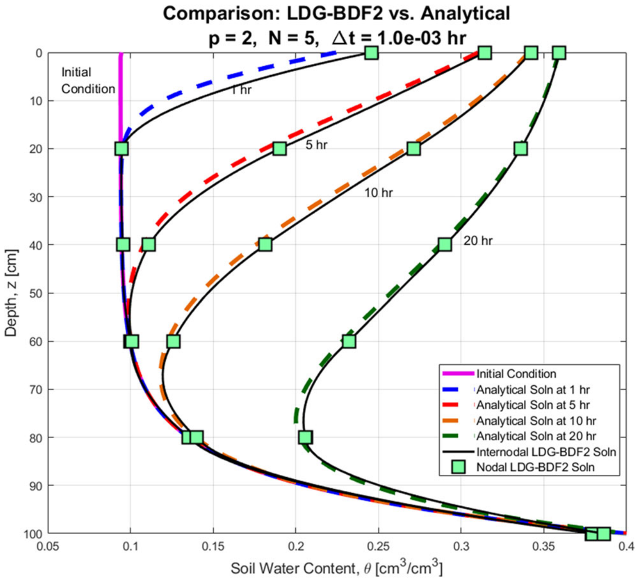

Fig. 4 Infiltration toward a Water Table: Comparison between LDG-BDF2 ($p = 2$, $N = 5$, $\epsilon = 10^{-6}$) and analytical solutions. L_2 errors at the four observation times (ascending order) are 0.0812, 0.0541, 0.0462 and 0.0347 respectively. Error is accumulated from incorrect convergence at the first time step due to an error tolerance of $\epsilon = 10^{-6}$. If $\epsilon = 10^{-3}$, the profiles would be equally accurate as those in Fig. 2

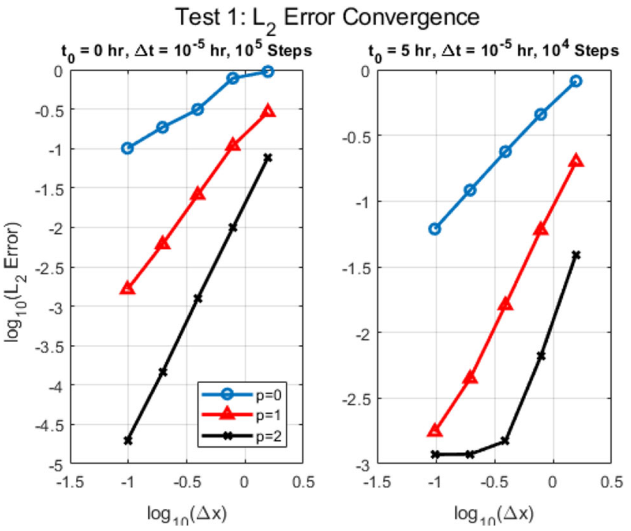

Fig. 5 L_2 error convergence from two different starting times. The slope of each curve over each refinement is listed in Table 1

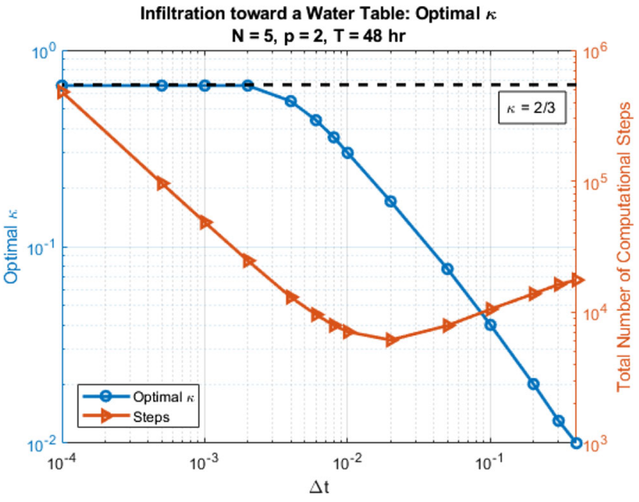

Fig. 6 Infiltration toward a Water Table: Optimal κ ($N = 5$, $p = 2$). Gradient of optimal κ before plateauing is roughly -0.8879 ($R^2 = 0.994$)

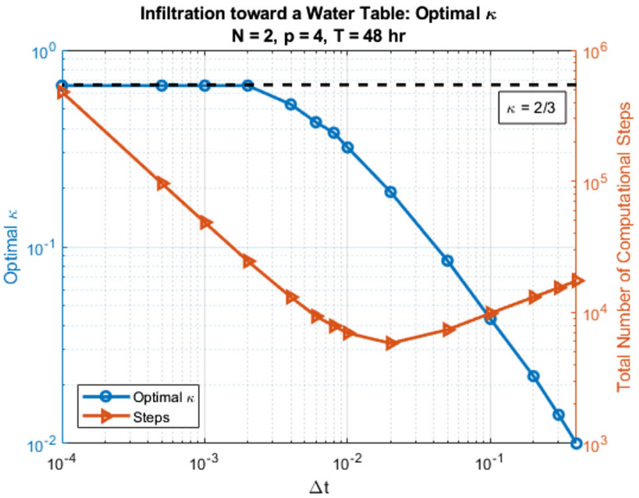

Fig. 7 Infiltration toward a Water Table: Optimal κ ($N = 2$, $p = 4$). Gradient of optimal κ before plateauing is roughly -0.8726 ($R^2 = 0.991$)

In supplement to the infiltration results above, some results for drainage are hereby provided. The exact solution for drainage is attained by swapping the values of q_A and q_B in Eq. 5.2, otherwise everything is kept unchanged. We set $N = 5$ and $p = 2$. Following the aforementioned method, we estimated and summarized optimal κ values for LDG-DT in Table 4. Figure 8 shows LDG-DT profiles generated with $\Delta t = 0.5$ hr; numerical results match the analytic results qualitatively well except for the upper limb at $t = 1$ hr, which can be remedied by either increasing the polynomial approximation or spatial resolution. Figure 9 presents change in optimal κ with respect to Δt.

Overall, LDG-DT can accurately converge at Δt several orders of magnitudes larger than LDG-BDF2, ultimately taking far fewer total computational steps (in this case, roughly 1/4 the number of steps) while being less sensitive to ϵ.

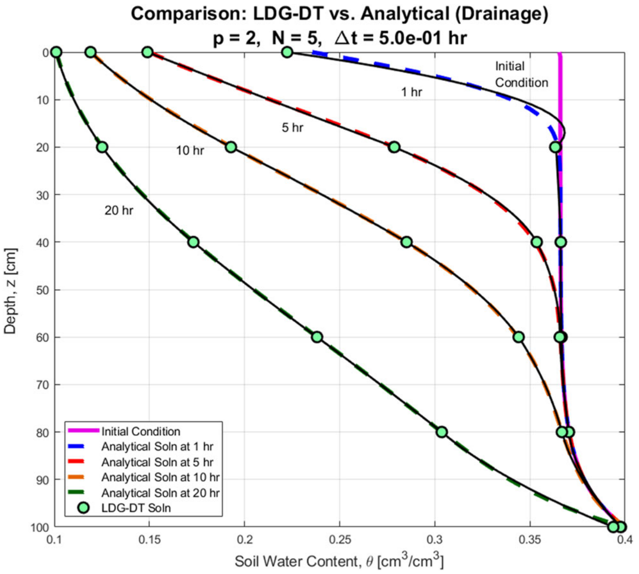

Fig. 8 Drainage toward a Water Table: Comparison between LDG-DT ($p = 2$, $N = 5$, $\epsilon = 10^{-6}$) and analytical solutions. L_2 errors at the four observation times (ascending order) are 0.0290, 0.0071, 0.0047 and 0.0094 respectively

5.2 Infiltration under constant surface moisture

We further verify our numerical result against an analytical solution derived by Hayek [28] for infiltration under a constant surface soil-water content based on the following variant of RE:

$$\frac{\partial S_e}{\partial t} + \frac{\partial}{\partial z}\left[K(S_e) - D(S_e)\frac{\partial S_e}{\partial z}\right] = 0, \tag{5.4}$$

where S_e, the degree of saturation, is given by the following θ-ψ constitutive relationship:

$$S_e = \frac{\theta - \theta_r}{\theta_s - \theta_r} = \exp\left(\frac{\alpha\psi}{n}\right),$$

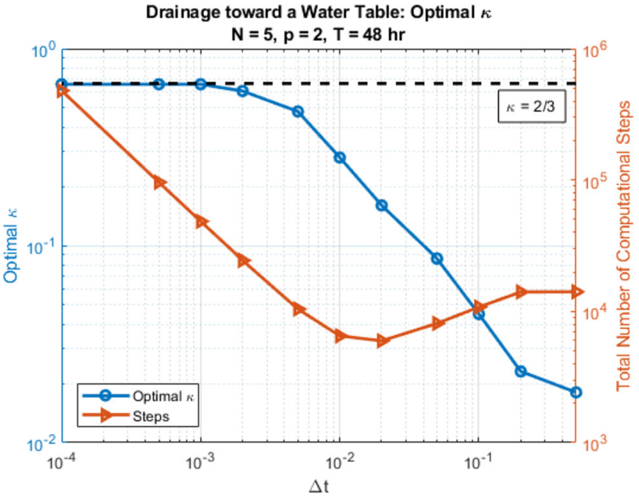

Fig. 9 Drainage toward a Water Table: Optimal κ ($N = 5$, $p = 2$). Gradient of optimal κ before plateauing is roughly -0.7054 ($R^2 = 0.984$)

Table 4 Drainage toward a Water Table: Estimated Optimal κ for LDG-DT and Comparison against LDG-BDF2 ($N = 5$, $p = 2$, $T = 48$ hr, $\kappa = \Delta\tau/\Delta t$)

Method	ϵ	Δt (hr)	κ	Steps	$\mathcal{E}_{L_2}$
DT	10^{-6}	0.5	0.018	14120	0.0261
		0.2	0.023	14070	0.0261
		0.1	0.045	10801	0.0261
		0.05	0.086	8106	0.0261
		0.02	**0.16**	**5972**	**0.0261**
		0.01	0.28	6513	0.0261
		0.005	0.48	10432	0.0261
		0.002	0.61	24598	0.0261
		0.001	0.66	48558	0.0261
		0.0005	0.66	96419	0.0261
		0.0001	0.66	480090	0.0261
BDF2	10^{-3}	≥ 0.004	–	Invalid	–
		0.002	–	24000	0.0261
		0.001	–	48000	0.0261
		0.0005	–	96000	0.0261
		0.0001	–	480000	0.0261

‘Steps’ is the total number of computational cycles/steps taken by the solver. For LDG-DT, this equals the summation of all pseudo-time steps in all physical-time steps; for LDG-BDF2, this equals the summation of all iterations in all physical-time steps. LDG-DT and LDG-BDF2 undergo the identical routine for spatial terms and only differ in the temporal derivatives. The most efficient run by the LDG-DT solver is emphasized in bold

‘$\mathcal{E}_{L_2}$’ is the L_2 error at T

‘Invalid’ marks unrealistic results, where at least one cell average θ value has exceeded the range of $[\theta_r,\ \theta_s]$ and led to unrealistic flux values where $n = 3.5$; $K(S_e)$ and $D(S_e)$ are respectively hydraulic conductivity and diffusivity, expressed as follows:

$$K(S_e) = \frac{K_s}{\theta_s - \theta_r} S_e^n,$$
$$D(S_e) = \frac{nK_s}{\alpha(\theta_s - \theta_r)} S_e^{n-1}.$$

The analytical solution of Eq. 5.4 at any time t in $z \in [0,\ z_f]$ is given by:

$$\theta = \theta_r + (\theta_* - \theta_r)\left[1 - \exp\left(\frac{\alpha(n-1)(z - \xi_0 - Vt)}{n}\right)\right].$$

Here, z_f is an arbitrary finite length (as the analytical solution is derived for an semi-infinite domain) which is set to 150 cm for our problem; top boundary condition (at $z = 0$) is $\theta = \theta_* - \delta$ for $\delta = 10^{-3}\theta_r$; below the wetting front, $\theta = \theta_r$ for the entire remaining domain. θ_* is set to θ_s; $\alpha = 1.0\ \text{cm}^{-1}$; $V = K_s/(\theta_s - \theta_r)$; ξ_0 is defined as follows:

$$\xi_0 = -\frac{n}{\alpha(n-1)} \ln\left[1 - \left(\frac{\theta_* - \delta - \theta_r}{\theta_* - \theta_r}\right)^{n-1}\right],$$

which is is simply the starting location of the wetting front. We set $\xi_0 = 50$ cm to lessen influence from the initial condition due to remarks by the author [28]. Lastly, $K_s = 1.0$ cm/hr, $\theta_s = 0.40$, and $\theta_r = 0.06$. This analytical solution represents a scenario where the soil surface is fully wet without accumulation of water. Within the soil, the depth above the wetting front would asymptotically approach full saturation as the wetting front travels indefinitely deeper.

LDG-DT settings are as follows. The top boundary conditions are:

$$\widehat{\psi}_{z=0} = 0\ \text{cm},$$
$$\left[\widehat{K} - \widehat{q}\right]_{z=0} = K_s.$$

The bottom boundary conditions are:

$$\widehat{\psi}_{z=100} = \psi^-_{z=100},$$
$$\widehat{K}_{z=100} = K^-_{z=100},$$
$$\widehat{q}_{z=100} = K^-_{z=100} \cdot r^-_{z=100}.$$

At internal element interfaces, the numerical fluxes are configured as follows:

$$\widehat{\psi}_z = \psi^-_z,$$
$$\widehat{K}_z = \frac{1}{2}\left(K^+_z + K^-_z\right) - \frac{\left|K'_{\max}\right|}{2}\left(\theta^+_z - \theta^-_z\right),$$
$$\widehat{q}_z = K^+_z \cdot r^+_z,$$

where $K'_{\max}$ is the local maximum partial derivative of K with respect to θ. Given that the soil profile underneath the wetting front is at exactly θ_r, undershooting of local solutions are expected. Therefore, the two slope limiters described in Section 3.2 are implemented separately.

Figures 10 and 11 present sample results predicted by LDG-DT. Observation times in the figures are selected to demonstrate issues in the minmod limiter, which fails to bound $\theta \in [\theta_r, \theta_s]$. In contrast, the bound-preserving limiter helps maintain realistic results (Fig. 12).

Fig. 10 Infiltration under Constant Surface Moisture: Comparison between LDG-DT and analytical solutions ($p = 1$, $N = 20$)

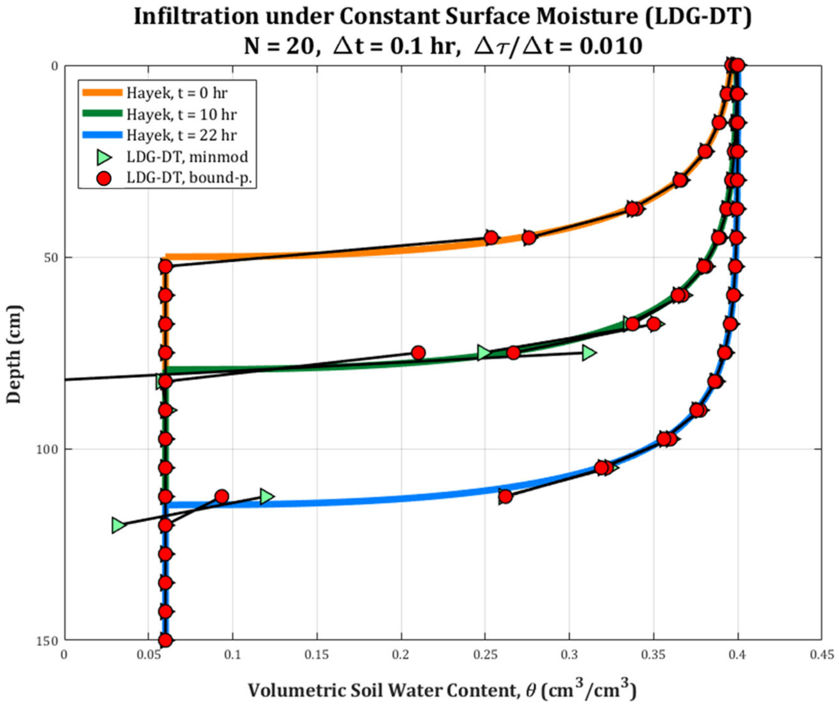

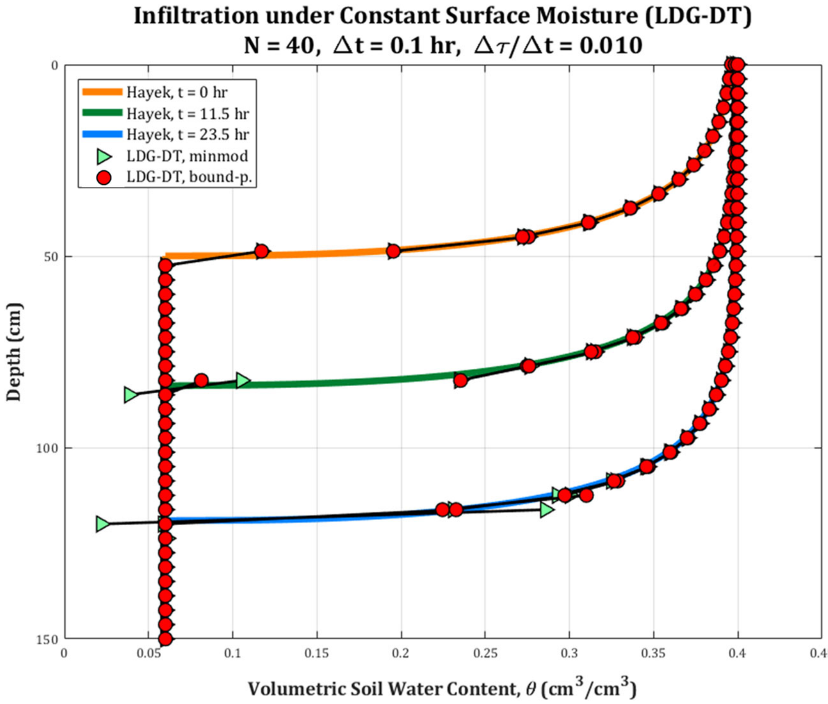

Fig. 11 Infiltration under Constant Surface Moisture: Comparison between LDG-DT and analytical solutions ($p = 1$, $N = 40$)

As before, the optimal κ for LDG-DT is estimated via trial and error, as summarized in Table 5 and illustrated in Fig. 13. Similar trends as in the first test problem are observed: the optimal κ increases as Δt decreases; an almost linear relationship in log-log scale is found between optimal κ and Δt for optimal $\kappa < 2/3$; the Δt at which optimal κ hits 2/3 is also where LDG-BDF2 starts to

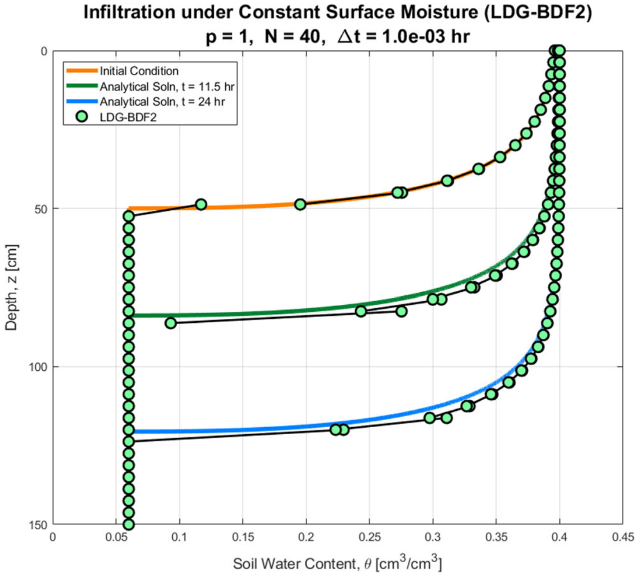

Fig. 12 Infiltration under Constant Surface Moisture: Comparison between LDG-BDF2 and analytical solutions ($p = 1$, $N = 40$). Overestimation of infiltration speed is caused by incompatible error tolerance

Table 5 Infiltration under Constant Surface Moisture: Estimated Optimal κ for LDG-DT and Comparison against LDG-BDF2 ($N = 20$, $p = 1$, $T = 24$ hr, $\kappa = \Delta\tau/\Delta t$)

Method	ϵ	Δt (hr)	κ	Steps	$\mathcal{E}_{L_2}$
DT	10^{-6}	0.4	0.065	4884	0.0586
		0.3	0.085	4888	0.0590
		0.2	0.12	4949	0.0595
		0.1	0.22	4859	0.0600
		0.05	**0.38**	**4695**	**0.0602**
		0.02	0.63	4828	0.0602
		0.01	0.65	6348	0.0602
		0.005	0.64	10142	0.0602
		0.002	0.66	23765	0.0602
		0.001	0.66	28105	0.0602
		0.0005	0.66	48713	0.0602
		0.0001	0.66	240501	0.0602
BDF2	10^{-3}	≥ 0.008	–	Invalid	–
		0.005	–	5316	0.7704
		0.002	–	12078	0.0896
		0.001	–	23999	0.0602
		0.0005	–	47999	0.0602
		0.0001	–	240000	0.0602

'Steps' is the total number of computational cycles/steps taken by the solver. For LDG-DT, this equals the summation of all pseudo-time steps in all physical-time steps; for LDG-BDF2, this equals the summation of all iterations in all physical-time steps. LDG-DT and LDG-BDF2 undergo the identical routine for spatial terms and only differ in the temporal derivatives. The most efficient run by the LDG-DT solver is emphasized in bold

'$\mathcal{E}_{L_2}$' is the L_2 error at T

'Invalid' marks unrealistic results, where at least one cell average θ value has exceeded the range of $[\theta_r,\ \theta_s]$

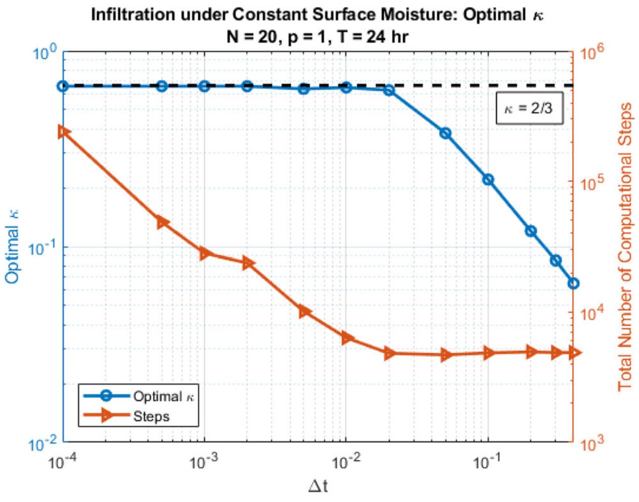

Fig. 13 Infiltration under Constant Surface Moisture: Optimal κ and Efficiency of LDG-DT ($N = 20$, $p = 1$). Gradient of optimal κ before plateauing is about -0.8250 ($R^2 = 0.996$)

produce satisfactory results on par with those of LDG-DT. Pertaining to error tolerance, once again it is discovered that $\epsilon < 10^{-3}$ causes non-convergence in LDG-BDF2, as shown in Fig. 12 where the solver is forced to advance in time with an inaccurate solution early on. In contrast, LDG-DT consistently returns the same result for $\epsilon \leq 10^{-6}$. For example, at $\Delta t = 0.05$ hr with $\kappa = 0.38$, the total number of computational steps is 4695 for $\epsilon = 10^{-6}$ and 17388 for $\epsilon = 10^{-10}$, but the L_2 error at $t = 24$ hr is 0.0602 regardless.

5.3 Horizontal infiltration under constant surface moisture

This problem is similar to the previous except infiltration occurs sideways as if water enters the soil through a vertical seepage face. This removes convection due to gravity and simplifies RE to a diffusion problem in an infinitely thin layer of soil, governed by

$$\frac{\partial \theta}{\partial t} = \frac{\partial}{\partial x}\left[D\big(\theta(\psi)\big)\frac{\partial \theta(\psi)}{\partial x}\right], \tag{5.5}$$

where x [L] is the horizontal spatial coordinate and D [L^2/T] is diffusivity. This is essentially the horizontal process in a multi-dimensional RE. Constitutive relationship for this problem is described by the Brooks-Corey model [29], which defines $D(\theta(\psi))$ as follows:

$$D\big(\theta(\psi)\big) = K(\psi)\frac{\partial \psi}{\partial \theta} = -\frac{K_s \psi_b}{\lambda(\theta_s - \theta_r)} S_e^{2+1/\lambda}.$$

Here ψ_b [L] is air-entry pressure head, λ [–] is pore-size distribution index, and S_e in unsaturated soil ($\psi < \psi_b$) can be expressed as

$$S_e = \frac{\theta - \theta_r}{\theta_s - \theta_r} = \left(\frac{\psi}{\psi_b}\right)^{-\lambda}.$$

Hayek [30] presents the analytical solution of Eq. 5.5 as follows:

$$\begin{aligned} x = {} & a\sqrt{D_s t}\left[m - nc(S_e - S_{ei})^n\right] \\ & \cdot (S_e - S_{ei})^{m-1} e^{-c(S_e - S_{ei})^n} + x_f(t), \end{aligned} \tag{5.6a}$$

$$\begin{aligned} x_f(t) = {} & -a\sqrt{D_s t}\left[m - nc(S_{e0} - S_{ei})^n\right] \\ & \cdot (S_{e0} - S_{ei})^{m-1} e^{-c(S_{e0} - S_{ei})^n}, \end{aligned} \tag{5.6b}$$

where t is the physical-time variable, D_s is diffusivity at full saturation, S_{ei} is degree of saturation of the initial condition, S_{e0} is degree of saturation based on the condition at the wet boundary ($S_{e0} = 1$ for this problem because the wet boundary is set to θ_s). All other parameters necessary for evaluation of Eq. 5.6 are included in Table 6.

LDG-DT settings are as follows. Initial condition of the entire 100-cm long domain is set to θ_i. Boundary conditions of the wet (left, −) end are:

$$\begin{aligned} \widehat{\psi}_{x=0} &= \psi_b, \\ \left[\widehat{K} - \widehat{q}\right]_{z=0} &= D\big(\theta(\psi_b)\big). \end{aligned}$$

Boundary conditions on the dry (right, +) end are:

$$\begin{aligned} \widehat{\psi}_{x=100} &= \psi^-_{x=100}, \\ \widehat{K}_{x=100} &= 0, \\ \widehat{q}_{x=100} &= D^-_{x=100} \cdot r^-_{x=100}. \end{aligned}$$

At internal element interfaces, the following numerical fluxes are applied:

$$\begin{aligned} \widehat{\psi}_x &= \psi^-_x, \\ \widehat{K}_x &= 0, \\ \widehat{q}_x &= D^+_x \cdot r^+_x. \end{aligned}$$

Table 6 Horizontal infiltration: soil parameters

Parameters	Sand	Sandy Loam
θ_r [cm^3/cm^3]	0.020	0.041
θ_i [cm^3/cm^3]	0.020	0.050
θ_s [cm^3/cm^3]	0.417	0.412
ψ_b [cm]	−7.26	−14.66
λ [–]	0.592	0.322
K_s [cm/hr]	21.00	2.59
a [–]	−0.15102	−0.11519
c [–]	−0.04263	−0.05732
m [–]	4.71929	5.90092
n [–]	5.00363	5.50562

Fig. 14 Horizontal infiltration: LDG-DT profiles in sand ($p = 1$, $N = 20$)

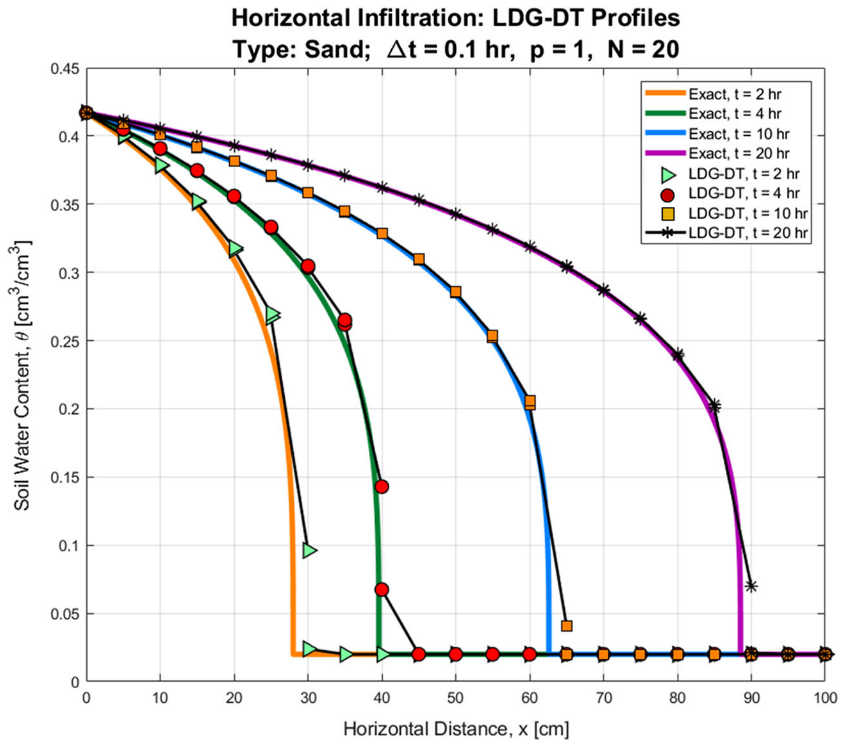

Due to $\theta_i \approx \theta_r$, the bound-preserving limiter is in place to prevent unrealistic solutions.

Figure 14 shows LDG-DT results using $N = 20$ and $\Delta t = 0.1$ hr in a sand domain. Overall agreement with the analytical solution is excellent and improves over time. Similar performance is seen in Fig. 15 for a sandy loam domain, where $N = 20$ and $\Delta t = 0.2$ hr. Sandy loam is less conductive than sand at high degrees of saturation, hence a larger physical-time step is allowed. In contrast, Fig. 16 shows slight overestimation of infiltration speed by LDG-BDF2 in early simulation. For evaluation of accuracy, due to difficulties in inverting (5.6) and expressing θ as a function

Fig. 15 Horizontal infiltration: LDG-DT profiles in sandy loam ($p = 1$, $N = 20$)

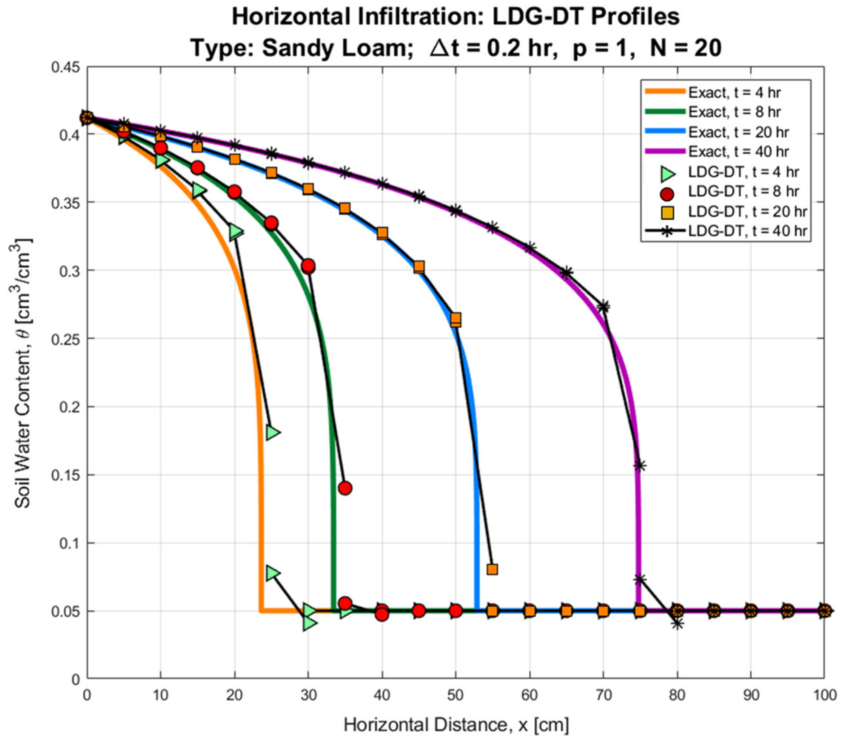

Fig. 16 Horizontal infiltration: LDG-BDF2 profiles in sand ($p = 1$, $N = 40$)

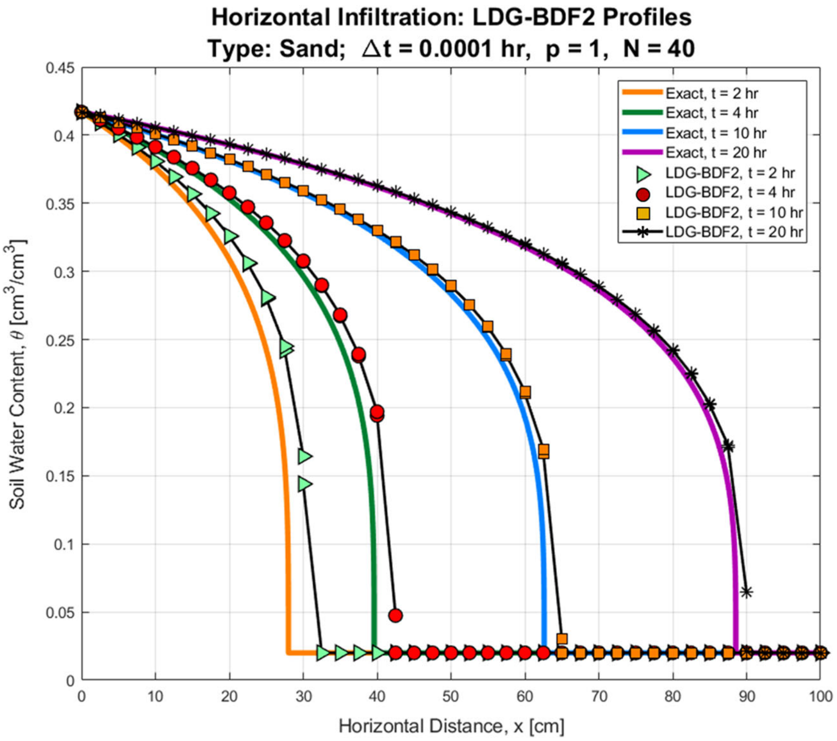

spatial coordinates, for the same θ profiles we plot the exact coordinates against the quadrature point coordinates and check how closely they align with the $y = x$ line in terms of the coefficient of determination, R^2.

Table 7 Horizontal infiltration under constant surface moisture: estimated optimal κ for LDG-DT (Sand, $N = 20$, $p = 1$, $T = 20$ hr, $\kappa = \Delta\tau/\Delta t$)

Method	ϵ	Δt (hr)	κ	Steps	R^2
DT	10^{-6}	0.1	0.013	32532	0.99982
		0.05	0.048	18564	0.99989
		0.02	0.11	16443	0.99990
		0.01	0.20	14624	0.99990
		0.005	**0.33**	**13653**	**0.99991**
		0.002	0.59	14821	0.99991
		0.001	0.63	22686	0.99991
		0.0005	0.66	41503	0.99990
		0.0002	0.66	100673	0.99991
		0.0001	0.66	200363	0.99991
BDF2	10^{-3}	$>$ 0.0001	–	Invalid	–
		0.0001	–	200358	0.99982

'Steps' is the total number of computational cycles/steps taken by the solver. For LDG-DT, this equals the summation of all pseudo-time steps in all physical-time steps; for LDG-BDF2, this equals the summation of all iterations in all physical-time steps. LDG-DT and LDG-BDF2 undergo the identical routine for spatial terms and only differ in the temporal derivatives. The most efficient run by the LDG-DT solver is emphasized in bold

'Invalid' marks incorrect results. In this case, at least one cell average θ value has exceeded the range of $[\theta_r,\ \theta_s]$

As before, estimated optimal κ are summarized in Tables 7 and 8, as well as plotted in Figs. 17 and 15. Optimal κ increases with decreasing Δt and is capped at about 2/3.

Table 8 Horizontal infiltration under constant surface moisture: estimated optimal κ for LDG-DT and Comparison against LDG-BDF2 (Sandy Loam, $N = 20$, $p = 1$, $T = 20$ hr, $\kappa = \Delta\tau/\Delta t$)

Method	ϵ	Δt (hr)	κ	Steps	R^2
DT	10^{-6}	0.1	0.052	9909	0.99972
		0.05	0.010	9294	0.99977
		0.02	0.22	8217	0.99978
		0.01	**0.36**	**7931**	**0.99978**
		0.005	0.56	8234	0.99979
		0.002	0.61	12617	0.99979
		0.001	0.66	21384	0.99979
		0.0005	0.66	40611	0.99979
		0.0002	0.66	100395	0.99979
		0.0001	0.66	200481	0.99979
BDF2	10^{-3}	$>$ 0.0001	–	Invalid	–
		0.0001	–	200012	0.99978

'Steps' is the total number of computational cycles/steps taken by the solver. For LDG-DT, this equals the summation of all pseudo-time steps in all physical-time steps; for LDG-BDF2, this equals the summation of all iterations in all physical-time steps. LDG-DT and LDG-BDF2 undergo the identical routine for spatial terms and only differ in the temporal derivatives. The most efficient run by the LDG-DT solver is emphasized in bold

'Invalid' marks incorrect results. In this case, at least one cell average θ value has exceeded the range of $[\theta_r,\ \theta_s]$

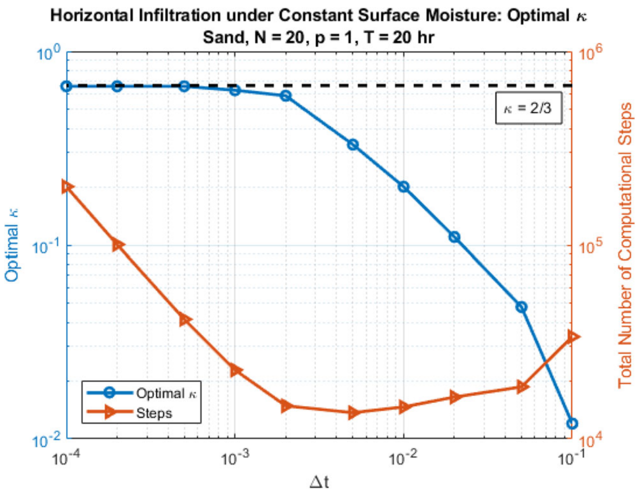

Fig. 17 Horizontal infiltration in sand: optimal κ

Unlike before, the trend prior to reaching 2/3 is not as linear; LDG-BDF2 does not immediately generate realistic results (i.e. θ would exceed the range of $[\theta_r,\ \theta_s]$) at the Δt where optimal κ first hits 2/3. For comparable outcomes, with a maximum Δt three orders of magnitude smaller than that of LDG-DT, LDG-BDF2 takes more than 10 times the computational steps (Fig. 18).

5.4 Ponded infiltration into a single layer

This problem simulates a scenario where a certain depth of water accumulates atop the soil and drives infiltration. Soil-water flow is characterized by the MVG model in Section 2. Hydraulic parameters of the soil column are provided in Table 9. Initial condition is set to a uniform pressure head of -100 cm. The top boundary conditions are

$$\begin{aligned}\widehat{\psi}_{z=0} &= 1\text{ cm},\\ \widehat{K}_{z=0} &= K_s,\\ \widehat{q}_{z=0} &= K^-_{z=0}\cdot r^-_{z=0}.\end{aligned}$$

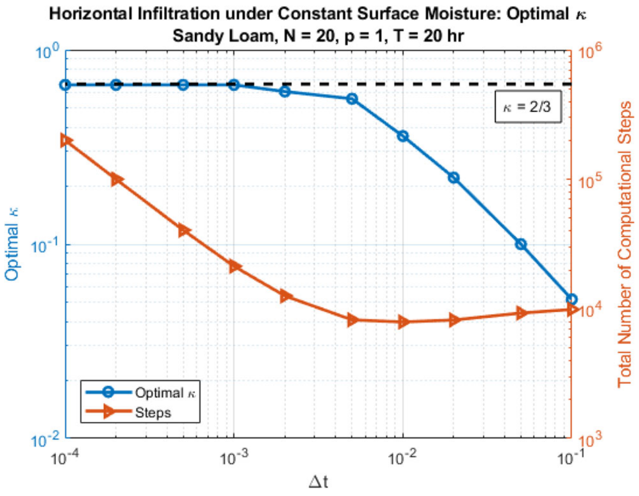

Fig. 18 Horizontal infiltration in sandy loam: optimal κ

Table 9 Single-layer ponded infiltration: soil parameters

Parameters	Value
θ_r [cm^3/cm^3]	0.078
θ_s [cm^3/cm^3]	0.430
α [1/cm]	0.036
n [–]	1.560
K_s [cm/day]	24.96
l [–]	0.5

The bottom boundary conditions are

$$\begin{aligned}\widehat{\psi}_{z=100} &= -100\text{ cm},\\ \widehat{K}_{z=100} &= K^-_{z=100},\\ \widehat{q}_{z=100} &= K^-_{z=100}\cdot r^-_{z=100}.\end{aligned}$$

At internal element interfaces, the following numerical fluxes are applied:

$$\begin{aligned}\widehat{\psi}_z &= \psi_z^-,\\ \widehat{K}_z &= \frac{1}{2}\left(K_z^+ + K_z^-\right) - \frac{|K'|}{2}\left(\theta_z^+ - \theta_z^-\right),\\ \widehat{q}_z &= K_z^+\cdot r_z^+,\end{aligned}$$

where $K'_{\max}$ is the local maximum derivative of K with respect to θ:

$$\begin{aligned}K' = \frac{\mathrm{d}K}{\mathrm{d}\theta} &= \frac{K_s l S_e^{l-1}}{\theta_s-\theta_r}\left[1-\left(1-S_e^{1/m}\right)^m\right]^2\\ &\quad - 2K_s Se^{l+1/m-1}\left[1-\left(1-S_e^{1/m}\right)^m\right]\\ &\quad \left(1-S_e^{1/m}\right)^{m-1}.\end{aligned}$$

We obtain HYDRUS-1D solution following Table 10 for qualitative comparison. The two slope limiting schemes introduced in Section 3.2 are also used separately in our solver. For all LDG-DT simulations, we stuck to the convergence criterion of $\left|\Delta w < 10^{-15}\right|$, but we also capped

Table 10 Single-layer ponded infiltration: HYDRUS settings

Parameters	Values
Soil depth [cm]	100
Number of nodes	101
Simulation Period [day]	0.5
Δt [day]	10^{-5}
Error Tolerance in θ	10^{-7}
Error Tolerance in ψ	10^{-3}
Maximum iteration	500
$\psi_{t=0}$ [cm]	-100
$\psi(z=0)$ [cm]	1
$\psi(z=100)$ [cm]	Free Drainage

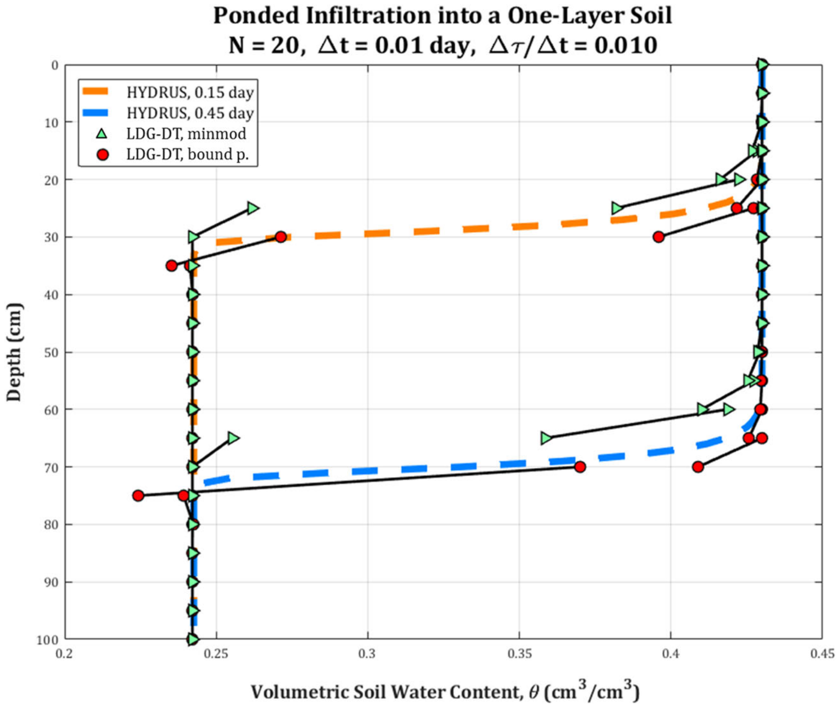

Fig. 19 Single-layer ponded infiltration: LDG-DT profiles for two slope limiting schemes and HYDRUS-1D solution

maximum inner iterations at 500 and forced the solver to advance in time should it fail to meet that precision.

Figure 19 presents LDG-DT profiles for $N = 20$, $\Delta t = 0.01$ day. Prediction of infiltration speed with the bound-preserving limiter roughly matches that by HYDRUS-1D. A bit of undershooting below the wetting front is visual because θ is still decently above θ_r, so the bound-preserving limiter remains inactive. Profiles generated with the minmod limiter are smoother in appearance, but most likely due to active adjustment of pressure gradient at almost all time, infiltration speed predicted with the minmod limiter is lower than that with the bound-preserving limiter. More graphical results are presented in Figs. 20 and 21. As spatial resolution increases, undershoots diminish in solution profiles with the bound-preserving limiter; the slowing down of infiltration speed becomes more apparent

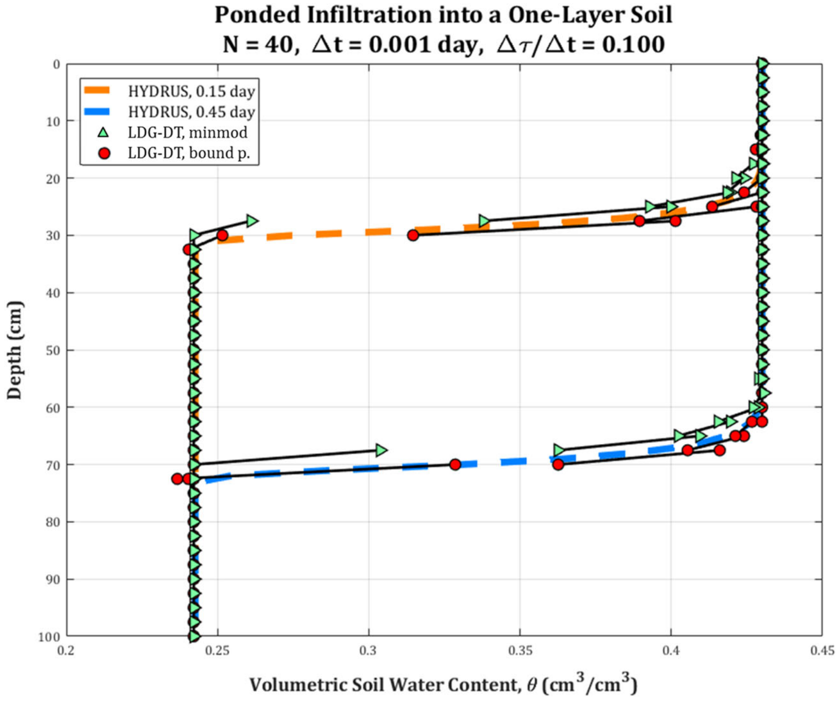

Fig. 20 Single-layer ponded infiltration: LDG-DT profiles for two slope limiting schemes and HYDRUS-1D solutions

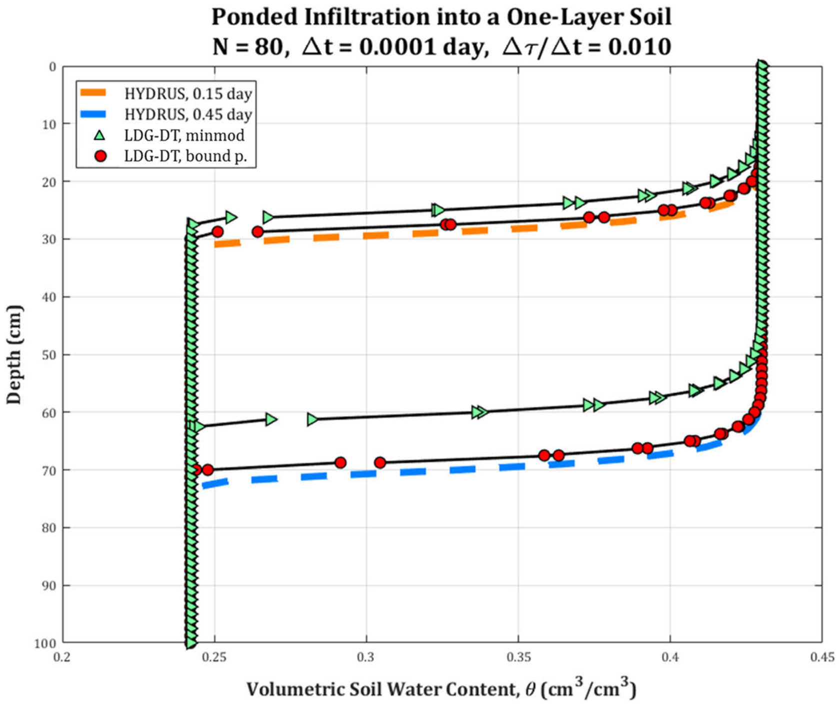

Fig. 21 Single-layer ponded infiltration: LDG-DT reference profiles for two slope limiting schemes and HYDRUS-1D solutions

using the minmod limiter, which likely makes its outcome less accurate. Using the solution profile with the bound-preserving limiter at $t = 1.25$ day in Fig. 21 as a reference, we report reference L_2 errors for $N = 10$, 20, and 40 ($\Delta t = 10^{-4}$ day for all) as 0.0667, 0.0449 and 0.0287, respectively.

We also present some BDF2 results for comparison. Figure 22 shows LDG-BDF2 predictions (with the

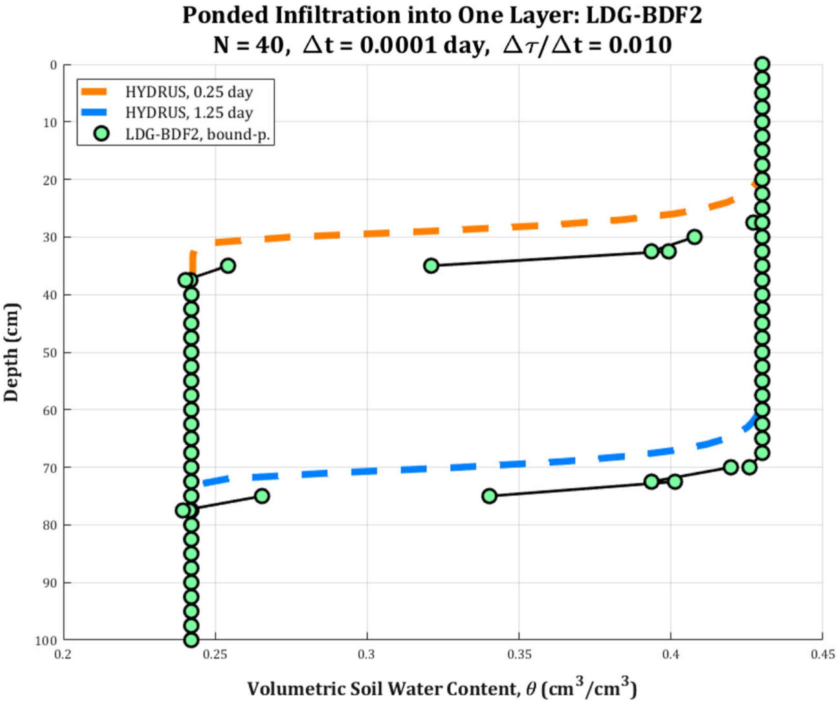

Fig. 22 Single-layer ponded infiltration: LDG-BDF2 profiles

bound-preserving limiter) at $N = 40$ and $\Delta t = 10^{-4}$ day. Similar to earlier tests, LDG-BDF2 estimation of infiltration speed is higher than LDG-DT. But more importantly, for the same spatial configurations, LDG-BDF2 requires Δt of roughly 2 orders of magnitudes smaller than that of LDG-DT in order to resolve reasonably. This is also the case for HYDRUS-1D, which implements backward Euler in time with a Picard iterative scheme to accelerate convergence. For example, HYDRUS-1D is able to converge using 21 nodes (equivalent to 20 elements) at $\Delta t = 10^{-3}$ day with an error tolerance of 10^{-4} in θ and 0.1 cm in ψ, but not when Δt is increased to 10^{-2} day even if the error tolerance is made more lenient.

5.5 Ponded infiltration into two layers

The setup is almost identical to the previous except the soil column consists of two layers with distinct hydraulic properties (clayey loam on top, sandy loam below). The characteristic relationships in Fig. 23 indicate that the upper layer is less conductive than the lower layer near saturation, but the opposite is true over a large range of ψ. Thus a jump in θ would be expected at the layer interface when both sides around the interface become equally conductive. Afterward, the upper layer would serve as a limiting barrier and prevent the lower layer from ever becoming fully saturated.

Soil-water flow is characterized by the MVG model in Section 2. Hydraulic parameters are provided in Table 11.

Table 11 Two-layer ponded infiltration: soil parameters

Parameters	Sandy Loam	Clayey Loam
θ_r	0.065	0.095
θ_s	0.410	0.410
α [1/cm]	0.075	0.019
n	1.890	1.310
K_s [cm/day]	106.1	6.24
l	0.5	0.5

Table 12 Two-layer ponded infiltration: HYDRUS settings

Parameters	Values
Clayey loam depth [cm]	0 – 40
Sandy loam depth [cm]	40 – 100
Number of nodes	101
Simulation Period [day]	1.25
Δt [day]	10^{-5}
Error Tolerance in θ	10^{-7}
Error Tolerance in ψ	10^{-3}
Maximum iteration	500
$\psi_{t=0}$ [cm]	-100
$\psi(z = 0)$ [cm]	1
$\psi(z = 100)$ [cm]	Free Drainage

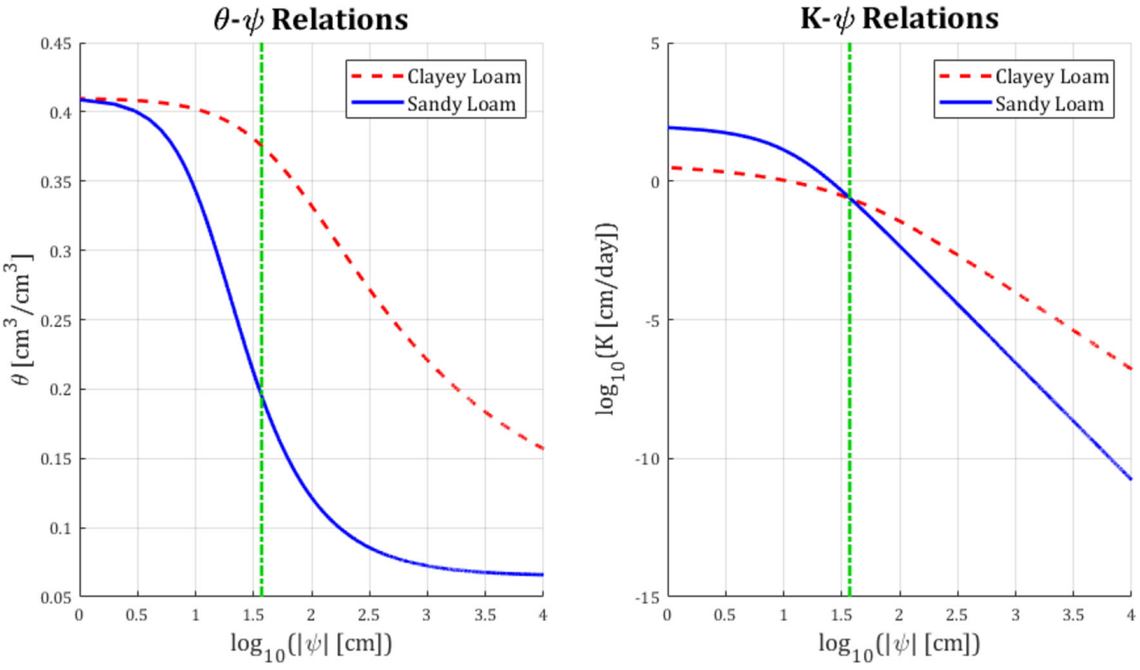

Fig. 23 Two-layer ponded infiltration: soil-water characteristic curves

Fig. 24 Two-layer ponded infiltration: solution profiles ($N = 20$)

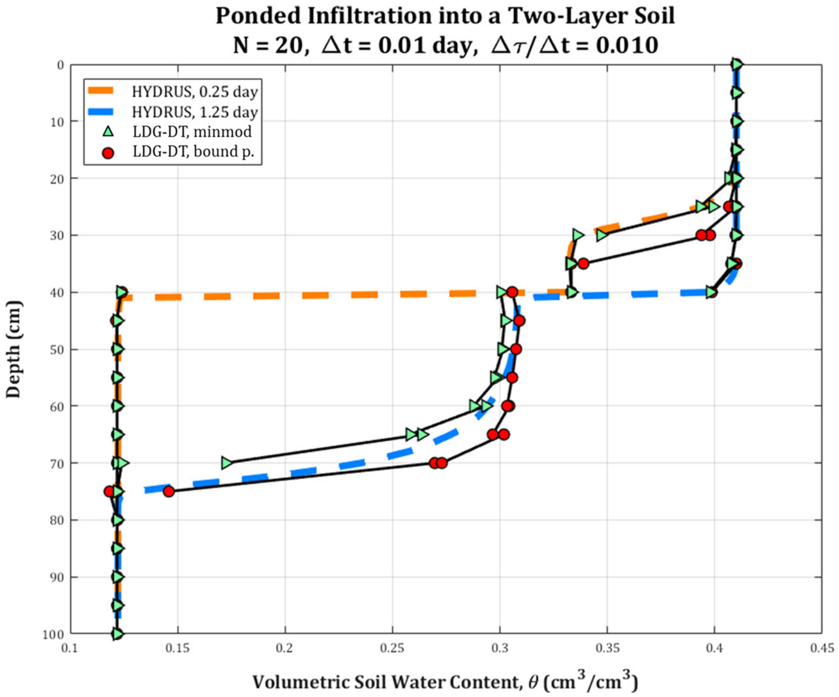

Initial and boundary conditions as well as internal numerical fluxes follow those in Section 5.4. HYDRUS-1D configurations are summarized in Table 12.

LDG-DT solutions were obtained using minmod and bound-preserving limiters separately. Figures 24 and 25 shows some results for different spatial resolutions. The observations in general are very similar to what is described in in Section 5.4. Note that because the lower layer is much less saturated than the upper layer, neither of the slope limiter is active in the lower layer. Reference solution profiles are shown in Fig. 26, generated with $N = 80$ and $\Delta t = 10^{-4}$. With the same time step size and using the

Fig. 25 Two-layer ponded infiltration: solution profiles ($N = 40$)

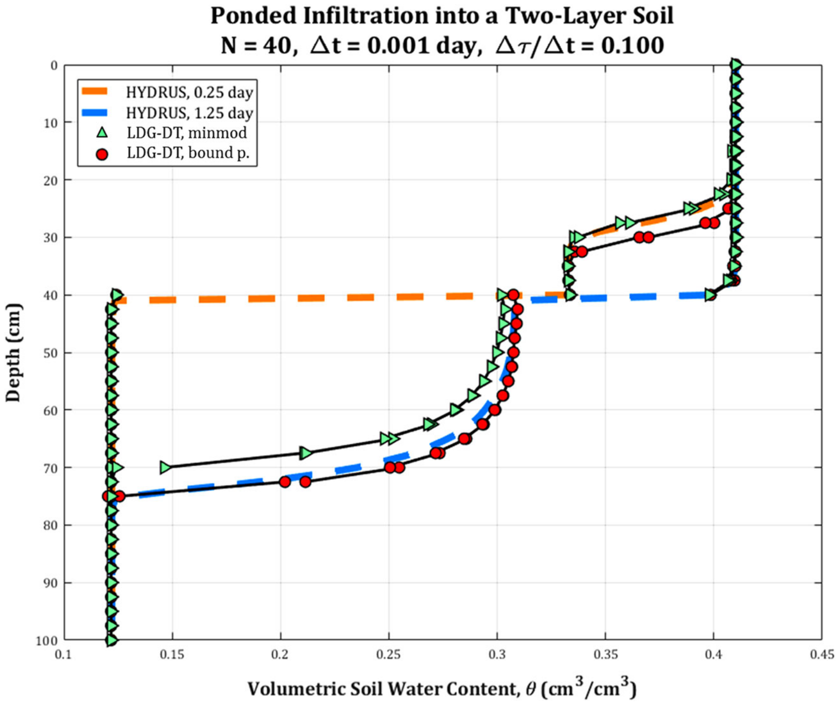

Fig. 26 Two-layer ponded infiltration: solutions profiles ($N = 80$)

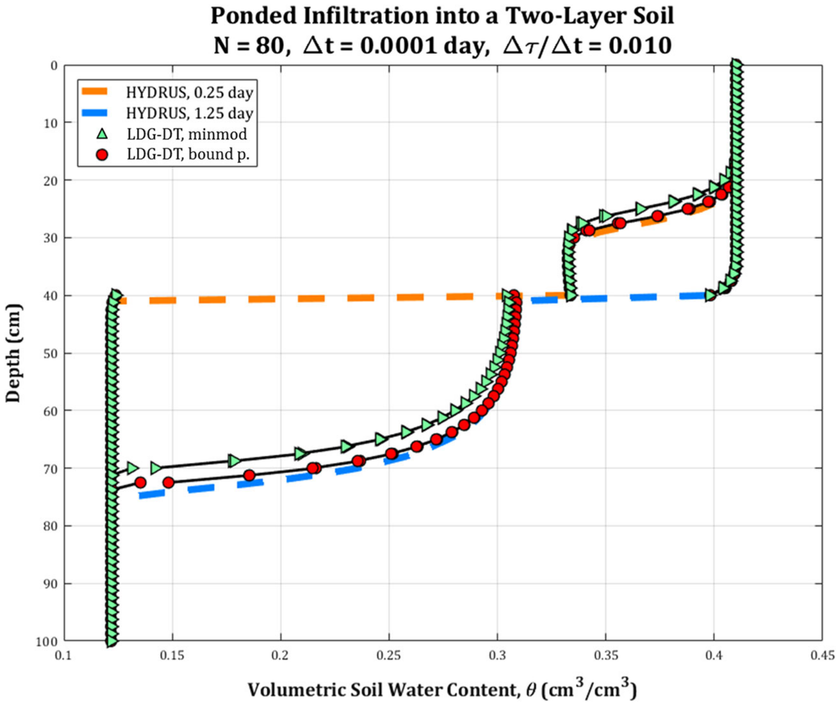

bound-preserving limiter, we report reference L_2 error of 0.0771, 0.0371 and 0.188 respectively for $N = 10$, 20, and 40.

Lastly, some LDG-BDF2 profiles are produced with the bound-preserving limiter and presented in Fig. 27. Once again, infiltration speed predicted by LDG-BDF2 is slightly higher than that by LDG-DT. LDG-BDF2 also requires Δt to be roughly 2 orders of magnitudes smaller than that of LDG-DT to resolve correctly. We also attempted running HYDRUS-1D with 21 nodes, which fails to converge with $\Delta t = 10^{-4}$ day until error tolerance is loosened to 10^{-2} in θ and 1 cm in ψ.

Fig. 27 Two-layer ponded infiltration: LDG-BDF2 profiles ($N = 40$)

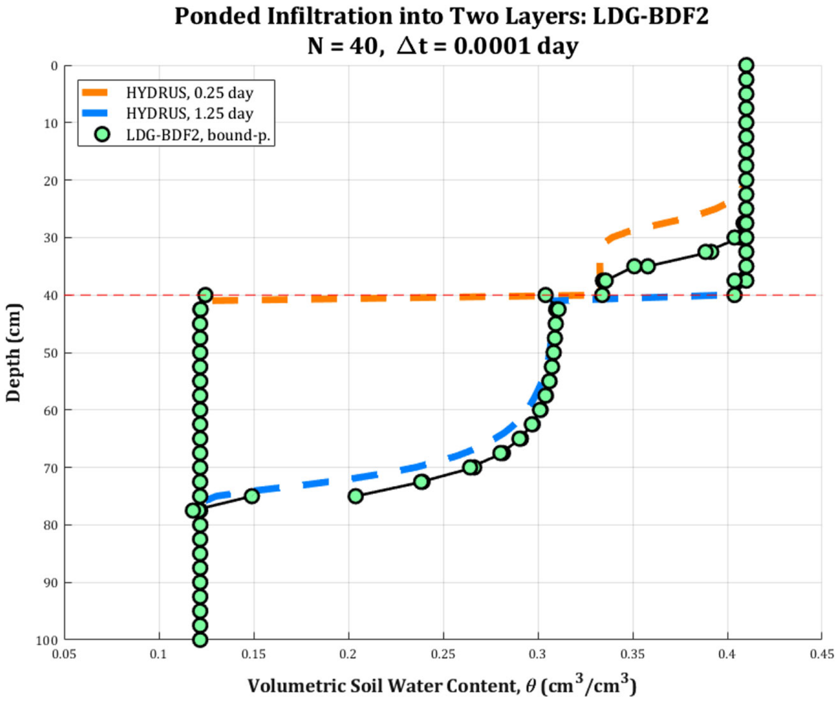

6 Conclusion

We solved 1D mixed-form RE with LDG-DT and demonstrated accuracy and robustness of our solver. Verification against analytical solutions shows the advantage of LDG in space to achieve comparable or even improved spatial accuracy under coarser resolutions via adjusting basis polynomial degree; compared to directly solving an implicitly discretized RE, the DT stepper largely expands the range of allowable physical-time step size without compromising on accuracy. DT is also found to be much more oblivious to shifts in error tolerance and thus far more consistent, unlike direct application of the implicit scheme which would require Δt to be compatible with error tolerance for satisfactory convegence. Qualitative comparison with HYDRUS-1D in ponded infiltration test problems shows that the LDG-DT solver can resolve to comparable results using much fewer elements and harsher error tolerance. Overall, LDG-DT appears very promising for numerical RE solutions. Currently, the optimization of DT parameters is via trial and error and has implied flaws in existing theories. Future study on dual-time efficiency would be extremely helpful.

Appendix A: LDG formulation supplements

A.1 Master element transform

To simplify implementation of Eq. 3.3, a master element $\widehat{\Omega} = \{\xi : \xi \in [-1, 1]\}$ is introduced. Any point on the master element can be linearly transformed to its corresponding point in Ω_j via:

$$z(\xi)|_{\Omega_j} = \frac{z_j + z_{j-1}}{2} + \frac{\Delta z_j}{2}\xi, \tag{A.1}$$

where z represents the spatial coordinates of points in Ω_j. Applying the master element transform to Eq. 3.3 yields:

$$\int_{\widehat{\Omega}} \frac{\partial \theta_h}{\partial t} v_{\theta,h} \frac{\mathrm{d}z}{\mathrm{d}\xi}, \mathrm{d}\xi = \int_{\widehat{\Omega}} \left(K(\psi_h) - q_h\right) \frac{\partial v_{\theta,h}}{\partial z} \frac{\mathrm{d}z}{\mathrm{d}\xi}\, \mathrm{d}\xi - \left(K(\psi_h) - q_h\right) v_{\theta,h}\Big|_{z_{j-1}}^{z_j}, \tag{A.2a}$$

$$\int_{\widehat{\Omega}} q_h v_{q,h} \frac{\mathrm{d}z}{\mathrm{d}\xi}\, \mathrm{d}\xi = \int_{\widehat{\Omega}} K(\psi_h) r_h v_{q,h} \frac{\mathrm{d}z}{\mathrm{d}\xi}\, \mathrm{d}\xi, \tag{A.2b}$$

$$\int_{\widehat{\Omega}} r_h v_{r,h} \frac{\mathrm{d}z}{\mathrm{d}\xi}\, \mathrm{d}\xi = -\int_{\widehat{\Omega}} \psi_h \frac{\partial v_{r,h}}{\partial z} \frac{\mathrm{d}z}{\mathrm{d}\xi}\, \mathrm{d}\xi + \psi_h v_{r,h}\Big|_{z_{j-1}}^{z_j}, \tag{A.2c}$$

where $\mathrm{d}z/\mathrm{d}\xi = \Delta z/2$ based on Eq. A.1. The tilde above v is removed to indicate that it is now a function of ξ.

A.2 Linear combinations of degrees of freedom and basis polynomials

In succession to Appendix A, all terms with a subscript 'h' in Eq. 3.3 are expressed as linear combinations of coefficients and basis polynomials:

$$v_{\chi,h} = \sum_{i=1}^{p+1} (\beta_\chi)_i \phi_i, \quad \chi \equiv \theta,\ q,\ \text{or}\ r$$

$$q_h = \sum_{i=1}^{p+1} (q_h)_i \phi_i = \mathbf{q}_h \cdot \Phi,$$

$$\theta_h = \sum_{i=1}^{p+1} (\theta_h)_i \phi_i = \mathbf{\Theta}_h \cdot \Phi,$$

$$\psi_h = \sum_{i=1}^{p+1} (\psi_h)_i \phi_i = \Psi_h \cdot \Phi,$$

where $(\beta_\chi)_i$ are arbitrary constant coefficients; ϕ_i is the $(i-1)$-th degree basis polynomial, for which Legendre polynomials orthogonal to one another over the interval $[-1,\ 1]$ are used; Φ is an array containing all ϕ_i for $i = 1,\ 2,\ \cdots,\ (p+1)$; $\mathbf{q}_h$, $\mathbf{\Theta}_h$ and Ψ_h are arrays containing degrees of freedom of their corresponding variables, q_h, θ_h and ψ_h. Conversion between θ_h and ψ_h can be made via the soil-water constitution relationships after converting the degrees of freedom to quadrature-point values. Gauss–Lobatto quadrature rule is implemented for numerical integration of the integrals in Eq. 3.3. The number of quadrature points per element is set to $n = \lceil (p+3)/2 \rceil$.

A.3 Elimination of arbitrary constant coefficients in the test functions

We use Eq. A.2a to demonstrate the procedure, which can be extended to the other equations with test functions. Starting with the index $i = 1$, by substituting $\left(v_{\theta,h}\right)_1 = (\beta_\theta)_1 \phi_1$ into Eq. A.2a for v_h, we obtain the following:

$$\int_{\widehat{\Omega}} \frac{\partial \theta_h}{\partial t} \left((\beta_\theta)_1 \phi_1\right) \frac{\mathrm{d}z}{\mathrm{d}\xi}\, \mathrm{d}\xi = \int_{\widehat{\Omega}} \left(K(\psi_h) - q_h\right) \frac{\partial \left((\beta_\theta)_1 \phi_1\right)}{\partial z} \frac{\mathrm{d}z}{\mathrm{d}\xi}\, \mathrm{d}\xi - \left(K(\psi_h) - q_h\right) \left((\beta_\theta)_1 \phi_1\right)\Big|_{z_{j-1}}^{z_j} \tag{A.4}$$

Because $(\beta_\theta)_1$ is a constant and appears in every term on both sides of the equation, it can be eliminated to leave only ϕ_1 in the original locations of $v_{\theta,h}$. This is applied to every i from 1 to $(p+1)$, giving us a total of $(p+1)$ equations (no longer with constant coefficients) and as many

ϕ_i. Therefore, the $(p+1)$ equations can be condensed into the following:

$$\int_{\widehat{\Omega}} \frac{\partial \theta_h}{\partial t} \Phi \frac{\mathrm{d}z}{\mathrm{d}\xi}\,\mathrm{d}\xi = \int_{\widehat{\Omega}} \left(K(\psi_h) - q_h\right) \frac{\partial \Phi}{\partial z} \frac{\mathrm{d}z}{\mathrm{d}\xi}\,\mathrm{d}\xi - \left(K(\psi_h) - q_h\right) \Phi \Big|_{z_{j-1}}^{z_j}, \tag{A.5}$$

where Φ is a $(p+1)$-by-1 array containing ϕ_i for $i = 1, 2, \cdots, (p+1)$.

A.4 Quadrature

Gauss–Lobatto quadrature is used to approximate definite integrals. To demonstrate, let $f(\zeta)$ and $g(\zeta)$ be two arbitrary functions defined over the domain of the master element, $\widehat{\Omega}$. The integral of their product over $\widehat{\Omega}$ can be approximate as follows:

$$\begin{aligned}
&\int_{\Omega} f(\zeta)\cdot g(\zeta)\,\mathrm{d}\Omega_e \\
&\approx \sum_{i=1}^{n} g(\zeta_i)\cdot w_i \cdot\ f(\zeta_i) \\
&= \begin{bmatrix} g(\zeta_1) \\ g(\zeta_2) \\ \vdots \\ g(\zeta_n) \end{bmatrix}^{\mathsf{T}} \begin{bmatrix} w_1 & 0 & \cdots & 0 \\ 0 & w_2 & \cdots & 0 \\ \vdots & \vdots & \ddots & \vdots \\ 0 & 0 & \cdots & w_n \end{bmatrix} \begin{bmatrix} f(\zeta_1) \\ f(\zeta_2) \\ \vdots \\ f(\zeta_n) \end{bmatrix}
\end{aligned}$$

where w_i and ζ_i $(i = 1, 2, \cdots, n)$ are the quadrature weights and points, respectively, for n-point Gauss–Lobatto quadrature rule. For an integrand in the form of a p-degree polynomial, the required n to produce identical result as exact integration is $n \geq \lceil (p+3)/2 \rceil$. For non-polynomial integrands, larger n generally improves accuracy.

A.5 Mass matrix

Taking advantage of quadrature rule and master element transform, the physical-time integral can be expressed as follows:

$$\begin{aligned}
\int_{\widehat{\Omega}} \frac{\partial \mathbf{\Theta}_h}{\partial t} \mathbf{\Phi}\,\mathrm{d}z &= \left[\int_{\widehat{\Omega}} \mathbf{\Phi}\mathbf{\Phi}\,\mathrm{d}z\right] \frac{\partial \mathbf{\Theta}}{\partial t} \\
&= \left[\mathbf{\Phi}^{\mathsf{T}}\mathbf{W}\mathbf{\Phi}\right] \frac{\partial \mathbf{\Theta}_h}{\partial t} \\
&= \mathbf{M}\frac{\partial \mathbf{\Theta}_h}{\partial t},
\end{aligned}$$

where $\mathbf{M}$ is the mass matrix.

A.6 Computational forms

Similar to the physical-time integral, the remaining terms in Eq. A.2 can be numerically approximated. In sum, the computational form of Eq. A.2 for the j-th element is:

$$\begin{aligned}
\frac{\partial \mathbf{\Theta}_h}{\partial t} &= \mathbf{A}\left(\mathbf{K} - \mathbf{q}\right) + \mathbf{B}^{-}_{z_j}\left(\widehat{\mathbf{K}} - \widehat{\mathbf{q}}\right)_{z_j} \\
&\quad - \mathbf{B}^{+}_{z_{j-1}}\left(\widehat{\mathbf{K}} - \widehat{\mathbf{q}}\right)_{z_{j-1}} && \text{(A.6a)} \\
\mathbf{q}_h &= \mathbf{L_2}\left(\mathbf{K}\cdot\mathbf{r}\right) && \text{(A.6b)} \\
\mathbf{r}_h &= -\mathbf{A}\Psi - \mathbf{B}^{-}_{z_j}\widehat{\Psi}_{z_j} \\
&\quad + \mathbf{B}^{+}_{z_{j-1}}\widehat{\Psi}_{z_{j-1}} && \text{(A.6c)}
\end{aligned}$$

where:

$$\begin{aligned}
\mathbf{A} &= \mathbf{M}^{-1}\frac{\partial \mathbf{\Phi}}{\partial \xi}^{\mathsf{T}}\mathbf{W}, \\
\mathbf{B}^{+}_{z_{j-1}} &= \frac{2}{\Delta z}\mathbf{M}^{-1}\mathbf{\Phi}^{+}_{z_{j-1}}, \\
\mathbf{B}^{-}_{z_j} &= \frac{2}{\Delta z}\mathbf{M}^{-1}\mathbf{\Phi}^{-}_{z_j}, \\
\mathbf{L_2} &= \mathbf{M}^{-1}\mathbf{\Phi}^{\mathsf{T}}\mathbf{W}, \\
\mathbf{M} &= \mathbf{\Phi}^{\mathsf{T}}\mathbf{W}\mathbf{\Phi}.
\end{aligned}$$

Further expanding some terms:

$$\mathbf{\Phi} = \begin{bmatrix} \phi_1(\xi_1) & \phi_2(\xi_1) & \cdots & \phi_{p+1}(\xi_1) \\ \phi_1(\xi_2) & \phi_2(\xi_2) & \cdots & \phi_{p+1}(\xi_2) \\ \vdots & \vdots & \ddots & \vdots \\ \phi_1(\xi_n) & \phi_2(\xi_n) & \cdots & \phi_{p+1}(\xi_n) \end{bmatrix}$$

$$\frac{\partial \mathbf{\Phi}}{\partial \xi} = \begin{bmatrix} \frac{\mathrm{d}\phi_1}{\mathrm{d}\xi}(\xi_1) & \frac{\mathrm{d}\phi_2}{\mathrm{d}\xi}(\xi_1) & \cdots & \frac{\mathrm{d}\phi_{p+1}}{\mathrm{d}\xi}(\xi_1) \\ \frac{\mathrm{d}\phi_1}{\mathrm{d}\xi}(\xi_2) & \frac{\mathrm{d}\phi_2}{\mathrm{d}\xi}(\xi_2) & \cdots & \frac{\mathrm{d}\phi_{p+1}}{\mathrm{d}\xi}(\xi_2) \\ \vdots & \vdots & \ddots & \vdots \\ \frac{\mathrm{d}\phi_1}{\mathrm{d}\xi}(\xi_n) & \frac{\mathrm{d}\phi_2}{\mathrm{d}\xi}(\xi_n) & \cdots & \frac{\mathrm{d}\phi_{p+1}}{\mathrm{d}\xi}(\xi_n) \end{bmatrix},$$

$$\mathbf{\Phi}^{+}_{z_i} = \begin{bmatrix} \phi_1(z_i^{+}) \\ \phi_2(z_i^{+}) \\ \vdots \\ \phi_{p+1}(z_i^{+}) \end{bmatrix}, \mathbf{\Phi}^{-}_{z_i} = \begin{bmatrix} \phi_1(z_i^{-}) \\ \phi_2(z_i^{-}) \\ \vdots \\ \phi_{p+1}(z_i^{-}) \end{bmatrix},$$

$$\mathbf{W} = \begin{bmatrix} w_1 & 0 & \cdots & 0 \\ 0 & w_2 & \cdots & 0 \\ \vdots & \vdots & \ddots & \vdots \\ 0 & 0 & \cdots & w_n \end{bmatrix},$$

$$\mathbf{f}\cdot\mathbf{g} = \begin{bmatrix} f(\xi_1)\cdot g(\xi_1) \\ f(\xi_2)\cdot g(\xi_2) \\ \vdots \\ f(\xi_n)\cdot g(\xi_n) \end{bmatrix}, \mathbf{f}_h = \begin{bmatrix} f_1 \\ f_2 \\ \vdots \\ f_{p+1} \end{bmatrix}.$$

The conversion between degrees of freedoms and solutions at quadrature points is via:

$$\mathbf{f} = \mathbf{\Phi}\mathbf{f}_h,$$
$$\mathbf{f}_h = \mathbf{L_2}\mathbf{f},$$

which closes (A.6).

Acknowledgements The authors would like to acknowledge the support of National Science Foundation grants CMMI-1563372 and ICER-1854991. All numerical results within this manuscript were generated from user-defined inputs included in the text and tables provided. No external data source was utilized.

Data Availability No external data source was accessed through the completion of this research. All settings for numerical results are provided within.

Declarations

Conflict of Interests The authors declare that they have no conflict of interest.

References

1. Richards, L.A.: Capillary conduction of liquids through porous mediums. Physics **1**(5), 318-333 (1931)
2. Farthing, M.W., Ogden, F.L.: Numerical solution of Richards; Equation: A review of advances and challenges. Soil Science Society of America Journal. The Soil Science Society of America, Inc. (2017)
3. Li, H., Farthing, M.W., Dawson, C.N., Miller, C.T.: Adaptive local discontinuous Galerkin approximation to Richards' equation. Advances in water resources. Adv. Water Resour. **30**(9), 1883–1901 (2007)
4. De Maet, T., Hanert, E., Vanclooster, M.: A fully-explicit discontinuous Galerkin hydrodynamic model for variably-saturated porous media. J. Hydrodyn. **26**(4), 594–607 (2014)
5. Cao, H., Yu, T., Yue, X.: Fully discrete IPDG–HMM for multiscale Richards equation of unsaturated flow in porous media. J. Comput. Appl. Math. **290**, 352–369 (2015)
6. Dolejší, V., Kuraz, M., Solin, P.: Adaptive higher-order space-time discontinuous Galerkin method for the computer simulation of variably-saturated porous media flows. Appl. Math. Model. **72**, 276–305 (2019)
7. Stormont, J.C., Anderson, C.E.: Capillary barrier effect from underlying coarser soil layer. J. Geotech. Geoenviron. **125**(8), 641–648 (1999)
8. Jameson, A.: Time dependent calculations using multigrid, with applications to unsteady flows past airfoils and wings. In: 10th Computational Fluid Dynamics Conference, p. 1596 (1991)
9. Arnone, A., Liou, M.S., Povinelli, L.A.: Multigrid time-accurate integration of Navier-Stokes equations. In: 11th Computational Fluid Dynamics Conference, p. 3361 (1993)
10. Cinnella, P., Lerat, A.: A fully implicit third-order scheme in time and space for compressible turbulent unsteady flow simulations. In: Proceedings of the ECCOMAS 2000 Conference (2000)
11. Klaij, C.M., van der Vegt, J.J., van der Ven, H.: Pseudo-time stepping methods for space–time discontinuous Galerkin discretizations of the compressible Navier–Stokes equations. J. Comput. Phys. **219**(2), 622–643 (2006)
12. Bogaard, T.A., Greco, R.: Landslide hydrology: from hydrology to pore pressure. Wiley Interdiscip. Rev. Water **3**(3), 439–459 (2016)
13. Ivanov, V.Y., Bras, R.L., Vivoni, E.R.: Vegetation]hydrology dynamics in complex terrain of semiarid areas: 1. A mechanistic approach to modeling dynamic feedbacks. Water Res. Res. **44**(3) (2008)
14. Ma, L., Ahuja, L., Nolan, B., Malone, R., Trout, T., Qi, Z.: Root zone water quality model (RZWQM2): Model use, calibration, and validation. Trans. ASABE **55**(4), 1425–1446 (2012)
15. Van Genuchten, M.T.: A closed-form equation for predicting the hydraulic conductivity of unsaturated soils 1. Soil Sci. Soc. Am. J. **44**(5), 892–898 (1980)
16. Cockburn, B., Shu, C.W.: The local discontinuous Galerkin method for time-dependent convection-diffusion systems. SIAM J. Numer. Anal. **35**(6), 2440–2463 (1998)
17. Aizinger, V., Dawson, C., Cockburn, B., Castillo, P.: The local discontinuous Galerkin method for contaminant transport. Adv. Water Resour. **24**(1), 73–87 (2000)
18. Xu, Z., Zhang, X.: Bound-preserving high-order schemes. In: Handbook of Numerical Analysis, vol. 18, pp. 81–102. Elsevier (2017)
19. Cockburn, B., Shu, C.W.: Runge–Kutta discontinuous Galerkin methods for convection-dominated problems. J. Sci. Comput. **16**(3), 173–261 (2001)
20. Kuzmin, D.: A new perspective on flux and slope limiting in discontinuous Galerkin methods for hyperbolic conservation laws. Comput. Methods Appl. Mech. Eng. **373**, 113569 (2021)
21. Chiew, J.J., Pulliam, T.H.: Stability analysis of dual-time stepping. In: 46th AIAA Fluid Dynamics Conference, p. 3963 (2016)
22. Šimunek, J., Šejna, M., Saito, H., Sakai, M., Van Genuchten, M.T.: Department of Environmental Sciences, University of California Riverside, Riverside, California, USA 315 (2008)
23. Celia, M.A., Bouloutas, E.T., Zarba, R.L.: A general mass]conservative numerical solution for the unsaturated flow equation. Water Resour. Res. **26**(7), 1483–1496 (1990)
24. Srivastava, R., Yeh, T.C.J.: Analytical solutions for one-dimensional, transient infiltration toward the water table in homogeneous and layered soils. Water Resour. Res. **27**(5), 753–762 (1991)
25. Gardner, W.R.: Some steady-state solutions of the unsaturated moisture flow equation with application to evaporation from a water table. Soil Sci. **85**(4), 228–232 (1958)
26. Irmay, S.: On the hydraulic conductivity of unsaturated soils. Eos, Trans. Am. Geophys. Union **35**(3), 463–467 (1954)
27. LeVeque, R.J.: Finite volume methods for hyperbolic problems, vol. 31. Cambridge University Press, Cambridge (2002)
28. Hayek, M.: An exact explicit solution for one-dimensional, transient, nonlinear Richards equation for modeling infiltration with special hydraulic functions. J. Hydrol. **535**, 662–670 (2016)
29. Brooks, R.H., Corey, A.T.: Hydraulic properties of porous media and their relation to drainage design. Trans. ASAE **7**(1), 26–28 (1964)
30. Hayek, M.: An efficient analytical model for horizontal infiltration in soils. J. Hydrol. **564**, 1120–1132 (2018)